Journal of The
Electrochemical Society

OPEN ACCESS

Physics-Based Continuum Modeling for an Aqueous Rechargeable Zn/MnO_2 Battery

To cite this article: John C. Bernard *et al* 2024 *J. Electrochem. Soc.* **171** 050502

View the article online for updates and enhancements.

You may also like

- Signatures of Massive Black Hole Merger Host Galaxies from Cosmological Simulations. I. Unique Galaxy Morphologies in Imaging
Jaeden Bardati, John J. Ruan, Daryl Haggard et al.

- Error scaling laws for kernel classification under source and capacity conditions
Hugo Cui, Bruno Loureiro, Florent Krzakala et al.

- Astrophysical Insights into Radial Velocity Jitter from an Analysis of 600 Planet-search Stars
Jacob K. Luhn, Jason T. Wright, Andrew W. Howard et al.

ECC-Opto-10 Optical Battery Test Cell:
Visualize the Processes Inside Your Battery!

EL-CELL®
electrochemical test equipment

✓ Battery Test Cell for Optical Characterization
Designed for light microscopy, Raman spectroscopy and XRD.

✓ Optimized, Low Profile Cell Design (Device Height 21.5 mm)
Low cell height for high compatibility, fits on standard samples stages.

✓ High Cycling Stability and Easy Handling
Dedicated sample holders for different electrode arrangements included!

✓ Cell Lids with Different Openings and Window Materials Available

Scan me!

Contact us:
+49 40 79012-734
sales@el-cell.com
www.el-cell.com

Sample Test (Side-by-Side Setup)
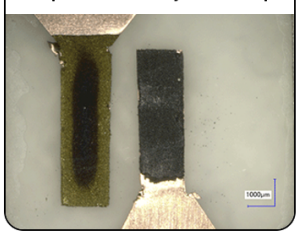

Sample Test (Face-to-Face Setup)
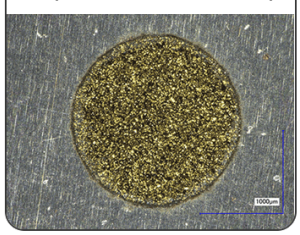

This content was downloaded from IP address 192.107.175.1 on 02/09/2025 at 14:02

Journal of The Electrochemical Society, 2024 **171** 050502

Physics-Based Continuum Modeling for an Aqueous Rechargeable Zn/MnO_2 Battery

John C. Bernard,[1,=] Zhongling Wang,[2,3,=] Shan Yan,[3,4] Esther S. Takeuchi,[2,3,4,5,*] Amy C. Marschilok,[2,3,4,5,] Kenneth J. Takeuchi,[2,3,4,5,**,z] and Alan C. West[1,6,*,z]**

[1]*Department of Chemical Engineering, Columbia University, New York, New York, 10027, United States of America*
[2]*Department of Materials Science and Chemical Engineering, Stony Brook University, Stony Brook, New York 11794, United States of America*
[3]*Institute of Energy: Sustainability, Environment, and Equity, Stony Brook University, Stony Brook, New York, 11794, United States of America*
[4]*Interdisciplinary Science Department, Brookhaven National Laboratory, Upton, NY 11973, United States of America*
[5]*Department of Chemistry, Stony Brook University, Stony Brook, New York, 11794, United States of America*
[6]*Department of Earth and Environmental Engineering, Columbia University, New York, New York, 10027, United States of America*

This study introduces a framework for modeling the aqueous Zn/MnO_2 rechargeable battery. A reaction system and a physics-based continuum model are proposed based on two reaction types, one involving insertion and the second related to dissolution and deposition of a solid reaction product. The model, fitted to empirical data, predicts voltage behavior and capacity limitations during cycling, identifying electrolytic zinc depletion as a limiting mechanism, depending on the original cell construction. The research suggests the need for further material characterization and reaction analysis, which will advance our understanding and facilitate the development of grid-scale energy storage solutions.

© 2024 The Author(s). Published on behalf of The Electrochemical Society by IOP Publishing Limited. This is an open access article distributed under the terms of the Creative Commons Attribution 4.0 License (CC BY, http://creativecommons.org/licenses/by/4.0/), which permits unrestricted reuse of the work in any medium, provided the original work is properly cited. [DOI: 10.1149/1945-7111/ad3f55]

Manuscript submitted February 16, 2024; revised manuscript received April 1, 2024. Published May 6, 2024.

Supplementary material for this article is available online

List of Symbols

General Model Symbols
z_j
Charge of species jC_j
Concentraion of species j (mol cm^{-3}))$C_{j,ref}$
Reference Concentraion of species j (mol cm^{-3})z_j
Charge of species $j\Phi_1$
Solid state potential (V)Φ_2
Solution potential (V)i_1
Solid state current density (A cm^{-2})i_2
Solution current density (A cm^{-2})$i_{applied}$
Applied current censity (A cm^{-2})i_k
Current density of reaction k (A cm^{-2})N_j
Solution flux of species j (mol cm^{-2}s^{-1})ε
Porosity of control volumeτ
Tortuosity of the control volumeD_j
Diffusion coefficient of species j (cm^{2}s^{-1})R
Ideal Gas Constant (8.314 J mol^{-1} K^{-1})T
Temperature (K)F
Faraday's constant (96,485 C mol^{-1})σ
Solid material conductivity (S cm^{-1})R_j
Molar Flux of species j generated by the reactions (mol cm^{-2} s^{-1})
$s_{j,k}$
Number of mols of species j in reaction k$n_{e,k}$
Number of electrons in reaction k$A_{react,k}$
Reaction area for reaction k (cm^2)Reaction Thermodynamics and Charge Transfer Kinetics Symbols
U_k
Reversible Potential of reaction k (V)U_k^{θ}
Reverisble Potential of reaction k at standard conditions (V)$\eta_{s,k}$
Overpotential of reaction k (V)$i_{0,k}$
Exchange current density of reaction k (A cm^{-2})$\alpha_{c,k}$
Cathodic transfer coefficient of reaction k$\alpha_{a,k}$
Anodic transfer coefficient of reaction k$k_{rxn,k}$
Kinetic constant of reaction k (A cm^{-2})Z
Ratio of Zinc to Manganese in the ZMC species$Z_{\min}$
Minimum ratio of Zinc to Manganese in the ZMC species$Z_{\max}$
Maximum Ratio of Zinc to Manganese in the ZMC species$\gamma_{Mn,k}$
Correction Term for Manganese reaction dependence

The consistent delivery of clean electrical energy remains a global challenge, exacerbated by the limitations of the current electric grid, which necessitates immediate consumption of generated electrical energy or risks its wastage or even damage to grid infrastructure.[1,2] The integration of electrical energy storage into the grid is increasingly recognized as a pivotal solution for enhancing grid reliability and resiliency, as well as for facilitating the incorporation of inherently intermittent renewable energy sources such as wind and solar.[3,4] In this context, stationary energy storage emerges as a critical and timely application for battery technologies.[5]

Candidate energy storage systems must be as cheap as possible, so that when they are coupled with power sources like wind and solar the total operation costs rivals that of current fossil fuel-based power. Additionally, these systems must be highly scalable to power large urban or industrial environments, possess long lifetimes as to be a reliable part of the electrical infrastructure, and be as safe and environmentally friendly as possible. Currently, aqueous batteries, such as those based on Zn/α-Manganese Dioxide (α-MnO_2) chemistries, are excellent candidates for stationary energy storage due to their low cost, scalability, and compatibility with Earth-abundant electrode materials.[6–9] Furthermore, batteries based on aqueous electrolytes generally tend to be safer when compared to their lithium-ion counterparts, which employ flammable non-aqueous organic electrolytes.[10,11]

Therefore, a mechanistic understanding of promising aqueous battery chemistries is critical for their optimization and large-scale deployment. Initial studies of Zn/MnO_2 with mildly acidic electrolytes have shown limited cycle life, but recently work has

[=]Equal contribution.
*Electrochemical Society Fellow.
**Electrochemical Society Member.
[z]E-mail: kenneth.takeuchi.1@stonybrook.edu; acw7@columbia.edu

demonstrated that the addition of aqueous manganese to the electrolyte during cell construction can extend cell lifetimes to thousands of cycles,[12] reigniting the interest in this chemistry for grid-scale storage. However, the electrochemical behavior of α-MnO_2 in aqueous systems has been a subject of ongoing research and debate. Multiple reaction mechanisms have been proposed, including H^+ and/or Zn^{2+} ion insertion reactions,[6,13–16] insertion induced conversion reactions,[6,12,14,16–26] and Mn^{2+} dissolution/deposition mechanisms.[11,27–37] Recent research seems to suggest that the manganese dissolution, which was initially viewed as a problematic degradation mode, is now part of the primary charge storage mechanism for this chemistry.

To explore and better understand the electrochemical and non-electrochemical reaction system, we have collected experimental data and developed a physics-based continuum model to simulate the behavior of the positive electrode during cycling. The model is validated against electrochemical and operando cycling data; through additional statistical parameter estimation, we tuned the model to better represent the observed electrochemical phenomena.

This model may help improve the current understanding of this electrochemical system and inform future experimental design to either further validate the proposed model or direct model adjustments and improvements. As the reaction mechanisms are yet to be fully characterized, this model may serve as a scaffold on which alternative or more nuanced reaction systems may be placed to improve the fidelity of the simulation tool. Future work will aim to utilize the model to optimize the chemistry in-silico, with the goal of pushing this system towards commercial viability in the long-term.

Methods

Material synthesis.—α-MnO_2 was hydrothermally synthesized by adapting a previously reported method.[38,39] Briefly, a solution of $KMnO_4$ in aqueous HCl was heated at 140 °C for 36 h in an autoclave, followed by washing, drying, and calcination at 300 °C for 6 h.[38,39]

Material characterization.—X-ray diffraction (XRD) was performed using a Rigaku Miniflex X-ray diffractometer with Cu K-alpha radiation (λ = 1.54056 Å) and Bragg-Brentano geometry. Water content was estimated from thermogravimetric analysis (TGA) using a TA instrument SDT Q600 under nitrogen.

Electrochemical methods.—The synthesized material and multi-wall carbon nanotubes (MWCNT) were combined to create the electrodes. Four coin-type electrochemical cells were constructed using an α-MnO_2/CNT cathode, 260 um thick glass fiber separator, zinc metal anode, and 2 M $ZnSO_4$ electrolyte. The cathodes were constructed using a 1:1 CNT to α-MnO_2 mass ratio, had thicknesses ranging from 325 um to 375 um, and had estimated porosities around 0.85. Galvanostatic cycling tests were performed using a BioLogic potentiostat within the voltage range of 1.1 to 1.7 V vs Zn at current densities of 50 mA g^{-1}, 100 mA g^{-1}, and 150 mA g^{-1}, 200 mA g^{-1} relative to the mass of pristine material. Galvanostatic Intermittent Titration Technique (GITT) testing involved intermittent application of discharge or charge current at 50 mA g^{-1} followed by rest steps. This procedure was done on two coin-type electrochemical cells identical to those tested during galvanostatic cycling. This procedure was iteratively applied throughout the entire charge/discharge process.

Model theory and governing equations.—A Newman-type continuum modeling framework was used to simulate the discharge behavior of the Zn/MnO_2 system studied in this work. The fundamental governing equations that were used as a base for this model are conservation of mass for the three primary electrolytic species considered (Zn^{2+}, Mn^{2+}, and SO_4^{2-} denoted by subscript j) given in Eq. 1, an electroneutrality condition for the three primary electrolytic species is given in Eq. 2, and a governing equation for solid-state (i_1) current given by Eq. 3. For simplicity of notation, the These equations were discretized using a finite-volume approach, and solved using Newman's published code.[40] This approach, while novel for the Zn/MnO_2 system described in this paper, has been widely used for modeling lithium-ion and other electrochemical systems.

$$\frac{\partial \varepsilon c_j}{\partial t} = -\nabla \bullet N_j + R_j \quad where \quad N_j = -\left(\frac{D_j \ \varepsilon}{\tau}\right)\nabla c_j - \frac{z_j D_j F \varepsilon}{RT\tau} c_j \nabla \Phi_2 \quad [1]$$

$$\sum_{j=All \quad Liquid \quad Species} z_j c_j = 0 \quad [2]$$

$$\nabla \bullet (i_1) = a i_{rxn} \quad where \quad i_s = -(1-\varepsilon)\sigma \nabla \Phi_1 \quad [3]$$

Two primary domains are considered in this model: the separator where no electrochemical reaction occurs, and the positive electrode where both electrochemical and chemical reactions are allowed to take place and where the composition of the material is allowed to evolve. The positive MnO_2 electrode will be referred to as the cathode throughout this work as is convention for rechargeable battery systems, and because this work deals principally with discharge behavior where the positive electrode is the acting cathode. Edge boundary conditions were applied at the zinc anode-separator interface and the cathode-current collector interface, and internal boundary conditions were applied to at the separator-cathode interface. At the zinc anode-separator interface, the boundary conditions where defined such that no solid state current (i_1) passes into the separator, that the ionic flux of Zinc ions ($N_{Zn^{2+}}$) carry 100% of the applied current ($i_{applied}$) while the flux of the other ions (N_{ZM} and $N_{SO_4^{2-}}$) are zero, and finally that the electrolyte potential at the interface is set to zero as the global potential reference for the simulation. At the cathode-current collector interface, boundary conditions were defined such that the solid-state current (i_1) is equivalent to the applied current ($i_{applied}$), that the electroneutrality condition holds, and that the flux of all species are zero at the current collector interface. The finite volume approximation allows simple implementation of internal boundary conditions; those being that the solid-state current (i_1) is zero because no electrons pass into or out of the separator, the flux of all electrolytic species on the separator side of the boundary is equivalent to the flux on cathode side of the boundary, and that conservation of charge holds. A diagram of this mathematical framework is given below in Fig. 1, and the full set of model equations can be found in Table I.

Model parameters used in the simulations can be grouped into three categories—those that remain conserved for all simulations (such as diffusion coefficients or charges of ions), those that vary from cell to cell and are simply measurable (such as thickness and porosity), and those that are systematically varied for statistical estimation of those parameters (such as kinetic constants). The first set is given in Table S.1, and the second set is given in Table S.2. For cell-specific parameters, all simulations are run so that the exact applied current, electrode thickness, electrode porosity, and volume fraction of constituent components match that of the experimentally tested electrode. This ensures that variations between different electrodes is accounted for by the model during parameter estimation.

Model parameter estimation.—There are a several parameters in this model that, while unknown, can be estimated by minimizing the residual sum of the squares when compared to experiment. As discussed in following sections, there are three primary electrochemical reactions we consider in the model, each of which has an yet unquantified kinetic constant ($k_{rxn,k}$). Additionally, one of these reactions deals with the insertion/extraction of zinc from a Zinc Manganese compound (ZMC), and maximum (Z_{max}) and minimum

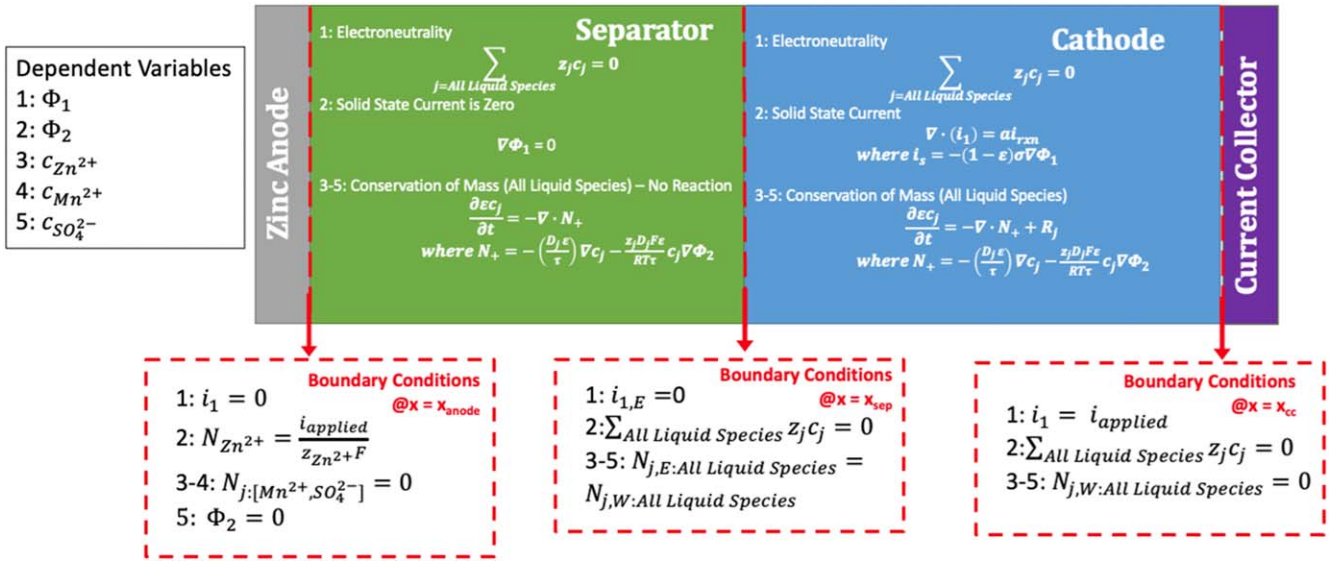

Figure 1. Continuum Model Diagram of the governing equations and boundary conditions of the Zn/MnO_2 physics-based model.

(Z_{min}) ratio of inserted zinc to manganese this ZMC species is not know with certainty. In two of the electrochemical reactions, the elementary reaction dependence on electrolytic manganese is not known, so correction terms ($\gamma_{Mn,k}$) are added and estimated. Finally, because electrolytic zinc is observed to limit the first electrochemical reaction's behavior, any depletion in electrolytic zinc due to the pH-driven formation of Zinc Hydroxide Sulfate (ZHS) must be estimated as well ($C_{Zn,initial}$). Because evidence points to little to no ZHS present at voltages above 1.45 volts,[12,25,28,29,35,37,41,42] this need not be done for any simulations beginning at the 1.7 V starting condition. Following parameter estimation methods developed by Brady et al.[43] and further improved by Mayilvahanan et al.,[44] one is able to generate mean estimates with uncertainty for each of these values. Experimentally, four different cells were tested, with an average mass of 4.35 mg of pristine active material per cathode. The active material mass and areal current density of each experimental electrode is given in Table S.2.

During the first discharge of a cell, it is posited that the only electrochemical reaction occurring is the dissolution of the pristine MnO_2 material—this means that the relevant unknown terms for the model in this state is the kinetic constant of Reaction 1 ($k_{rxn,1}$), the initial electrolytic zinc concentration ($C_{Zn,initial}$), and the zinc correction terms ($\gamma_{Mn,1}$) in Reaction 1. By simulating this one reaction and comparing the results to data from an initial galvanostatic discharge at a variety of C-rates, each parameter can be simultaneously estimated. To do this, one must first define a possible range for each constant. The $k_{rxn,1}$ parameter was sampled in log space to cover orders of magnitudes of kinetic constants, the $C_{Zn,initial}$ parameter was sampled from the initial concentration each cell was made at (2 M Zn^{2+}) to a 50% depletion due to spontaneous formation of ZHS during cell construction, and the $\gamma_{Mn,1}$ parameter was sampled between 0 and 1, representing no dependence to a maximum dependence on electrolytic zinc respectively as defined below. Using Sobol sampling,[45] simulations were run to uniformly cover this 3-dimensional parameter space.

From the simulated discharge curves, two metrics are used to optimize the model. The first is the residual sum of squares (RSS) between each discharge curve and the experimental discharge curve—in practice this is done by comparing the simulated and experimental discharge voltage at every increment of experimental gravimetric capacity. The second is the square of the difference between the simulated and experimental gravimetric capacity. Using both metrics allows matching of both the reaction capacity and voltage profile. By assuming a Gaussian distribution on the kinetic constant parameter, Kernel Density Estimation[46] (KDE) was employed to generate a 3-dimentional probability density function (PDF). Using a Bayesian approach[47] and an assumption of uniform priors across the sampling interval for all parameters, a PDF was calculated based on the capacity matching. Next, this PDF calculated from the capacity matching metric is treated as a prior and the PDF calculated from the voltage matching metric is treated a likelihood, thus generating *a posterior* distribution for all three values based on both metrics.

To estimate the remaining unknown parameters ($k_{rxn,2}$, $k_{rxn,3}$, Z_{min}, Z_{max}, and $\gamma_{Mn,2}$) a similar procedure is employed. By the 5th discharge, the reaction plateau associated with Reaction 1 has disappeared due to the irreversible nature of the reaction—therefore one can compare to the 5th experimental discharge of each cell and only simulate Reaction 2 and 3. The kinetic constants are estimated in log space, $\gamma_{Zn,2}$ was sampled from 0 to 1, and the z-terms are estimated on a scale from 0 to 1 atoms of zinc per atom of manganese in the ZMC compound. Again, fit metrics for both the capacity and voltage profile are employed, but in this case for two reactions, resulting in four total metrics used for these estimates. Each is used to generate a probability distribution function, which are combined using a Bayesian approach to yield one final 5-dimension PDF in the same manner as described above.

For both sets (Reaction 1 parameters and Reaction 2 and 3 parameters), a two-pass methodology was used, allowing for more precise estimates of the parameters. Following the generation of the initial PDF fit to both the capacity and voltage metrics over a wide sampling space, the parameter sampling space was redefined to within 2 standard deviations of the mean values (representing a 95% confidence interval). This new parameter space was then resampled, re-simulated, and used to create a new likelihood PDF in an identical method to that described above, but with the much denser sampling data within our 95% confidence interval. Using the initial PDF distributions generated during the first wide sampling pass as prior distributions, we generated updated posterior distributions that are reported in the following sections. This methodology allows for the sampling of a wider initial parameter space, while still allotting a high simulation density near the mean values without requiring excess computation.

Results

Material characterization.—The XRD pattern for the as-synthesized pristine material aligns well with the reference pattern (PDF# 042–1348), as shown in Fig. S1(a). Potassium α-MnO_2 displays a

Table I. Model governing equations and boundary conditions.

	Governing equation in Anode	Governing equation in Cathode	Zn Anode/Separator Interface	Separator/Cathode Interface	Cathode/Current Collector Interface
Electroneutrality	$\sum_{j=[Zn^{2+},Mn^{2+},SO_4^{2-}]} z_j C_j = 0$	$\sum_{j=[Zn^{2+},Mn^{2+},SO_4^{2-}]} z_j C_j = 0$	$\sum_{j=[Zn^{2+},Mn^{2+},SO_4^{2-}]} z_j C_j = 0$	$\sum_{j=[Zn^{2+},Mn^{2+},SO_4^{2-}]} z_j C_j = 0$	$\sum_{j=[Zn^{2+},Mn^{2+},SO_4^{2-}]} z_j C_j = 0$
Solid State Current	$\nabla\Phi_1 = 0$	$\nabla\bullet(i_1) = R_I$	$i_1 = 0$	$i_{1,E} = i_{1,W}$	$i_1 = i_{applied}$
Zn^{2+} conservation of mass	$\frac{\partial \varepsilon C_{Zn^{2+}}}{\partial t} = -\nabla\bullet N_{Zn^{2+}}$	$\frac{\partial \varepsilon C_{Zn^{2+}}}{\partial t} = -\nabla\bullet N_{Zn^{2+}} + R_{Zn^{2+}}$	$N_{Zn^{2+}} = \frac{i_{applied}}{z_{Zn^{2+}F}}$	$N_{Zn^{2+},E} = N_{Zn^{2+},W}$	$N_{Zn^{2+},W} = 0$
Mn^{2+} conservation of mass	$\frac{\partial \varepsilon C_{Mn^{2+}}}{\partial t} = -\nabla\bullet N_{Mn^{2+}}$	$\frac{\partial \varepsilon C_{Mn^{2+}}}{\partial t} = -\nabla\bullet N_{Mn^{2+}} + R_{Mn^{2+}}$	$N_{Mn^{2+}} = 0$	$N_{Mn^{2+},E} = N_{Mn^{2+},W}$	$N_{Mn^{2+},W} = 0$
SO_4^{2-} conservation of mass	$\frac{\partial \varepsilon C_{SO_4^{2-}}}{\partial t} = -\nabla\bullet N_{SO_4^{2-}}$	$\frac{\partial \varepsilon C_{SO_4^{2-}}}{\partial t} = -\nabla\bullet N_{SO_4^{2-}} + R_{SO_4^{2-}}$	$\Phi_2 = 0$	$N_{SO_4^{2-},E} = N_{SO_4^{2-},W}$	$N_{SO_4^{2-},W} = 0$
where	$N_j = -\left(\frac{D_j \varepsilon}{\tau}\right)\nabla C_j - \frac{z_j D_j F \varepsilon}{RT\tau} C_j \nabla\Phi_2$	$i_1 = -(1-\varepsilon)\sigma\nabla\Phi_1$	$R_j = \sum_k \frac{s_{j,k}}{n_{e,k}F} i_k * A_{react,k}$		

Reaction 1: Pristine Material Dissolution Reaction: $KMn_8O_{16} + 21H_2O + \frac{64}{3}Zn^{2+} + \frac{16}{3}SO_4^{2-} + 15e^- \rightarrow 8Mn^{2+} + K^+ + \frac{16}{3}Zn_4SO_4(OH)_6\bullet 5H_2O_{(s)}$

Nernst Equation

$$U_1 = U_1^\theta + \frac{RT}{F}\ln\left[\left(\frac{C_{Zn^{2+}}}{C_{Zn^{2+},ref}}\right)^{\left(\frac{64}{45}\right)}\left(\frac{C_{SO_4^{2-}}}{C_{SO_4^{2-},ref}}\right)^{\left(\frac{16}{45}\right)}\left(\frac{C_{Mn^{2+}}}{C_{Mn^{2+},ref}}\right)^{-\gamma_{Mn,1}\left(\frac{8}{15}\right)}\right]$$

$$i_{o,1} = k_{rxn,1}\left(\frac{C_{Zn^{2+}}}{C_{Zn^{2+},ref}}\right)^{\alpha_{a,1}\left(\frac{64}{45}\right)}\left(\frac{C_{SO_4^{2-}}}{C_{SO_4^{2-},ref}}\right)^{\gamma_{Mn,1}\alpha_{a,1}\left(\frac{16}{45}\right)}\left(\frac{C_{Mn^{2+}}}{C_{Mn^{2+},ref}}\right)^{-\alpha_{c,1}\left(\frac{8}{15}\right)}$$

where $\eta_{s,1} = \phi_1 - \phi_2 - U_1$

Butler-Volmer

$$i_1 = i_{o,1}\left(\exp\left(\frac{\alpha_{a,1}F\eta_{s,1}}{RT}\right) - \exp\left(\frac{-\alpha_{c,1}F\eta_{s,1}}{RT}\right)\right)$$

Reaction 2: ZMC Material Dissolution/Deposition Reaction: $Zn_{z_{\min}}MnO_2 + \left(\frac{8}{3} - z_{\min}\right)Zn^{2+} + \frac{2}{3}SO_4^{2-} + 16/3H_2O + 2(z_{\min}-1)e^- \rightleftharpoons Mn^{2+} + \frac{2}{3}Zn_4SO_4(OH)_6\bullet 5H_2O_{(s)}$

Nernst Equation

$$U_2 = U_2^\theta + \frac{RT}{F}\ln\left[\left(\frac{C_{Zn^{2+}}}{C_{Zn^{2+},ref}}\right)^{\frac{\left(\frac{8}{3}-z_{\min}\right)}{2(1-z_{\min})}}\left(\frac{C_{SO_4^{2-}}}{C_{SO_4^{2-},ref}}\right)^{\frac{\left(\frac{2}{3}\right)}{2(1-z_{\min})}} \times \left(\frac{C_{Mn^{2+}}}{C_{Mn^{2+},ref}}\right)^{\gamma_{Mn,2}\frac{-1}{2(1-z_{\min})}}\right]$$

$$i_{o,2} = k_{rxn,2}\left(\frac{C_{Zn^{2+}}}{C_{Zn^{2+},ref}}\right)^{\frac{\alpha_{a,2}\left(\frac{8}{3}-z_{\min}\right)}{2(1-z_{\min})}}\left(\frac{C_{SO_4^{2-}}}{C_{SO_4^{2-},ref}}\right)^{\frac{\alpha_{a,2}\left(\frac{2}{3}\right)}{2(1-z_{\min})}}\left(\frac{C_{Mn^{2+}}}{C_{Mn^{2+},ref}}\right)^{\gamma_{Mn,2}\frac{-1*\alpha_{c,2}}{2(1-z_{\min})}}$$

where $\eta_{s,2} = \phi_1 - \phi_2 - U_2$

Butler-Volmer

$$i_2 = i_{o,2}\left(\exp\left(\frac{\alpha_{a,2}F\eta_{s,2}}{RT}\right) - \exp\left(\frac{-\alpha_{c,2}F\eta_{s,2}}{RT}\right)\right)$$

Reaction 3: ZMC Insertion/Extraction Reaction: $Zn_{z-y}MnO_2 + yZn^{2+} + 2ye^- \rightleftharpoons Zn_zMnO_2$

Nernst Equation

$$U_3 = f_{empirical\ spline}(\theta) + \frac{RT}{F}\ln\left[\left(\frac{C_{Zn^{2+}}}{C_{Zn^{2+},ref}}\right)^{\frac{1}{2}}\right] \quad where\ \theta = \frac{z - z_{\min}}{z_{\max} - z_{\min}}$$

$$i_{o,3} = k_{rxn,3}\left(\frac{C_{Zn^{2+}}}{C_{Zn^{2+},ref}}\right)^{\frac{\alpha_{a,3}}{2}} z^{\alpha_{a,3}}(z_{\max} - z)^{\alpha_{c,3}}$$

where $\eta_{s,3} = \phi_1 - \phi_2 - U_3$

Butler-Volmer

$$i_3 = i_{o,3}\left(\exp\left(\frac{\alpha_{a,3}F\eta_{s,3}}{RT}\right) - \exp\left(\frac{-\alpha_{c,3}F\eta_{s,3}}{RT}\right)\right)$$

2 × 2 tunnel structure, featuring Mn octahedra as tunnel walls and K^+ ions occupying the tunnel center.[48] Mn positioned at the tunnel walls exhibits a mixed Mn (III) / Mn (IV) oxidation state due to the presence of the charge balancing K^+ ions. Water content was assessed via Thermogravimetric Analysis (TGA), illustrated in Fig. S1(b), using a previously reported method.[49,50]

Electrochemical and chemical reaction system.—As outlined in the introduction, the precise charge storage mechanism in mildly acidic electrolytes is still a matter of debate. However, this uncertainty need not stop us from developing a model of this system. By selecting a set of mechanisms that seems to best explain current experimental observations of the system, real behavior of the system can be closely approximated; as more is learned about these reaction mechanisms, the model can be updated without compromising the general model basis outlined in the work.

A reaction system initially outlined by Wu et al.,[51] gives a four reaction system that seems to capture most of experimental effects reported to date. The first reaction deals with the dissolution of the pristine α-MnO_2, which is mildly potassiated; this is believed to be a mostly, if not completely, irreversible process. This reaction is given by Eq. 4a below. Experimentally, this reaction is supported by the notion that the initial discharge behavior is one large plateau, and it is akin to the 3rd voltage plateau seen in subsequent discharges. Furthermore, that third voltage plateau disappears steadily though initial cycling, suggesting that this is an irreversible process that fully consumes the pristine material over the first few cycles.

$$KMn_8O_{16} + 32H^+ + 15e^- \rightarrow 8Mn^{2+} + K^+ + 16H_2O \qquad [4a]$$

The second reaction proposed by the Wu et al.[51] suggests that during charge a new Zinc Manganese Compound (ZMC) is deposited. As charge continues, a third electrochemical reaction is observed where the Zinc in the ZMC compound is extracted. These reactions are given by Eqs. 5a and 6, respectively. Evidence for the insertion/extraction behavior of Eq. 6 is given by Lee et al.[35] where the authors show that zinc content within the ZMC species increases and decreases in line with this proposed mechanism. Additionally, the voltage profile of this section of the discharge curve is characteristic of an insertion-type mechanism as described and common in Lithium-ion systems.[52–56] The observation by Wu et al.[29] that manganese concentration reversibly rises and falls during cycling supports the assertion that ZMC reversible dissolves during discharge, thus raising electrolytic manganese concentrations, and deposits during charge, thus decreasing the manganese concentration.

$$Zn_xMnO_2 + 4H^+ + 2(1-x)e^- \rightleftharpoons Mn^{2+} + (x)Zn^{2+} + 2H_2O \qquad [5a]$$

$$Zn_{z-y}MnO_2 + yZn^{2+} + 2ye^- \rightleftharpoons Zn_zMnO_2 \qquad [6]$$

The entire process is illustrated by Fig. 2, which shows the voltage curve for a cell's initial discharge, charge, and second discharge. Overlayed onto this figure are the associated reaction labels illustrating the full mechanism. For the purpose of clarity throughout this work, the pristine material dissolution reaction is referred to as Reaction 1, the dissolution/deposition reaction of the ZMC species as Reaction 2, and the zinc insertion/extraction reaction as Reaction 3.

The last relevant reaction of this electrochemical system is the reversible formation of a solid zinc-hydroxide-sulfate (ZHS) species that is observable only when the cell is in a discharged state below ~1.4 volts.[12,25,28,29,35,37,41,42] It is believed that during the dissolution of either the pristine or ZMC compound, the consumption of hydrogen ions (or similarly the production of hydroxide ions) drives the pH of the electrolyte near the reaction surface toward a more basic regime. This pH swing is responsible for the formation of ZHS. The ZHS species then dissolves during charge as the reverse electrochemical reaction drives the local pH to more acidic conditions. This reaction is given by Eq. 7 below.

$$Zn_4SO_4(OH)_6{\bullet}5H_2O_{(s)} \longrightarrow 4Zn^{2+}_{(aq)} + SO^{2-}_{4(aq)} + 5H_2O + 6OH^-_{(aq)} \qquad [7]$$

Notably, modeling dynamic localized pH gradients is difficult, particularly when the effect of pH on the kinetics or voltage characteristics on any of these proposed reactions remains mostly unquantified, though studies have begun to elucidate the impact pH may have on this system.[57–59] The authors have ignored more complex and nuanced phenomena that might arise from this pH dependence by lumping the ZHS formation reaction into the electrochemical dissolution reactions of the pristine material and ZMC. This gives two new reaction equations, Eqs. 4b and 5b, that are implemented into the model along with the insertion reaction.

$$KMn_8O_{16} + 21H_2O + \tfrac{64}{3}Zn^{2+} + \tfrac{16}{3}SO_4^{2-} + 15e^- \rightarrow 8Mn^{2+} + K^+ + \tfrac{16}{3}Zn_4SO_4(OH)_6{\bullet}5H_2O_{(s)} \qquad [4b]$$

$$Zn_{z_{max}}MnO_2 + \left(\tfrac{8}{3} - z_{max}\right)Zn^{2+} + \tfrac{2}{3}SO_4^{2-} + \tfrac{16}{3}H_2O + 2(1-z_{max})e^- \rightleftharpoons Mn^{2+} + \tfrac{2}{3}Zn_4SO_4(OH)_6{\bullet}5H_2O_{(s)} \qquad [5b]$$

Kinetic and thermodynamic relationships.—To fully implement these three electrochemical reactions, an effort must be made to derive the form of the Butler-Volmer kinetics and thermodynamic characteristics of each. Typically, this is done for each elementary reaction step, but absent knowledge of the precise elementary reactions occurring, one can utilize the full stoichiometric reactions denoted by Eqs. 4b, 5b and 6 as a starting point. As Reactions 1 and 2 are conversion reactions, which don't exhibit dependence on some inserted species, this can be done using a conventional approach. By representing the kinetics in the generic Butler-Volmer Form given by Eq. 8, kinetic considerations can be lumped into an exchange current density (i_0) dependent on the reaction (denoted by subscript j).

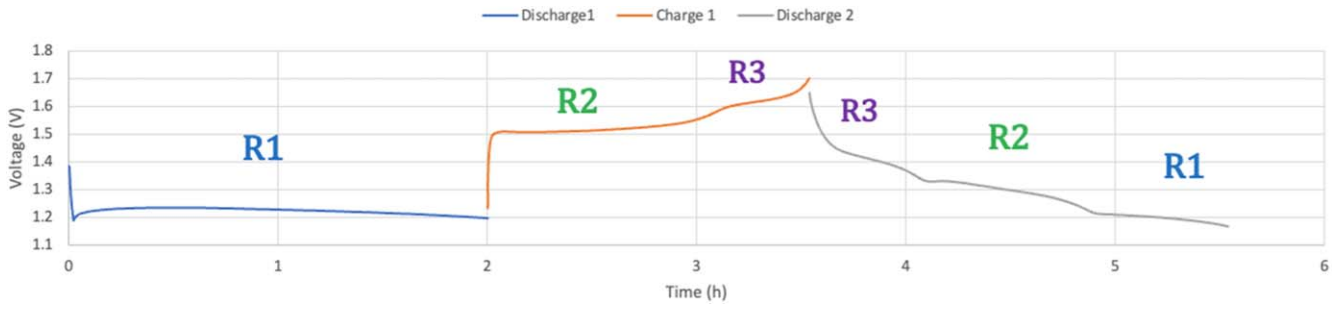

Figure 2. Initial Charge/Discharge Cycles with modeled reactions. Experimental data cycling performed at a rate of 150 mA g^{-1}.

$$i_j = i_{o,j}\left[\exp\left(\frac{\alpha_{a,j}F\eta_s}{RT}\right) - \exp\left(-\frac{\alpha_{c,j}F\eta_s}{RT}\right)\right] \quad [8]$$

Where the overpotential (η_s) is equivalent to the difference between the solid potential (Φ_1) and solution potential (Φ_2) minus the reaction open circuit potential (U). For the pristine material dissolution, the exchange current density is given by Eq. 9 and the open circuit potential is given by Eq. 10.

$$i_{o,1} = Fk_{a,1}^{-\alpha_{a,1}}k_{c,1}^{\alpha_{c,1}}\left(\frac{C_{Zn^{2+}}}{C_{Zn^{2+},ref}}\right)^{\alpha_{a,1}\left(\frac{64}{45}\right)}\left(\frac{C_{SO_4^{2-}}}{C_{SO_4^{2-},ref}}\right)^{\alpha_{a,1}\left(\frac{16}{45}\right)} \times\left(\frac{C_{Mn^{2+}}}{C_{Mn^{2+},ref}}\right)^{-\alpha_{c,1}\left(\frac{8}{15}\right)}\left(\frac{C_{K^+}}{C_{K^+,ref}}\right)^{-\alpha_{c,1}\left(\frac{1}{15}\right)} \quad [9a]$$

$$U_1 = U_1^\theta + \frac{RT}{F}\ln\left[\left(\frac{C_{Zn^{2+}}}{C_{Zn^{2+},ref}}\right)^{\left(\frac{64}{45}\right)}\left(\frac{C_{SO_4^{2-}}}{C_{SO_4^{2-},ref}}\right)^{\left(\frac{16}{45}\right)}\left(\frac{C_{Mn^{2+}}}{C_{Mn^{2+},ref}}\right)^{-\left(\frac{8}{15}\right)}\left(\frac{C_{K^+}}{C_{K^+,ref}}\right)^{-\left(\frac{1}{15}\right)}\right] \quad [10a]$$

Equations 9a and 10a are derived simultaneously, and the dependence of each concentration dependent block of the equation is raised to the power of the stoichiometric coefficient over the total electrons in each reaction. Additionally, because electrolytic potassium is such a small component of the system—even when the pristine material has fully dissolved—the authors have chosen to ignore the corresponding terms in the above equations. Finally, Faraday's constant (F) and the cathodic and anodic kinetic constants (k_c and k_a, respectively) can be combined into a singular kinetic constant (k_{rxn}) with units of $mAcm^{-2}$, giving us revised relationships in Eqs. 9b and 10b that are implemented in the model.

$$i_{o,1} = k_{rxn,1}\left(\frac{C_{Zn^{2+}}}{C_{Zn^{2+},ref}}\right)^{\alpha_{a,1}\left(\frac{64}{45}\right)}\left(\frac{C_{SO_4^{2-}}}{C_{SO_4^{2-},ref}}\right)^{\alpha_{a,1}\left(\gamma_{Mn,1}\frac{16}{45}\right)}\left(\frac{C_{Mn^{2+}}}{C_{Mn^{2+},ref}}\right)^{-\alpha_{c,1}\left(\frac{8}{15}\right)} \quad [9b]$$

$$U_1 = U_1^\theta + \frac{RT}{F}\ln\left[\left(\frac{C_{Zn^{2+}}}{C_{Zn^{2+},ref}}\right)^{\left(\frac{64}{45}\right)}\left(\frac{C_{SO_4^{2-}}}{C_{SO_4^{2-},ref}}\right)^{\left(\gamma_{Mn,1}\frac{16}{45}\right)}\left(\frac{C_{Mn^{2+}}}{C_{Mn^{2+},ref}}\right)^{-\left(\frac{8}{15}\right)}\right] \quad [10b]$$

Similarly, the corresponding relationships for the dissolution and deposition of the ZMC species are given by Eqs. 11 and 12.

$$i_{o,2} = k_{rxn,2}\left(\frac{C_{Zn^{2+}}}{C_{Zn^{2+},ref}}\right)^{\frac{\alpha_{a,2}\left(\frac{8}{3}-z_{\max}\right)}{2(1-z_{\max})}} \left(\frac{C_{SO_4^{2-}}}{C_{SO_4^{2-},ref}}\right)^{\frac{\alpha_{a,2}\gamma_{Mn,2}\left(\frac{2}{3}\right)}{2(1-z_{\max})}}\left(\frac{C_{Mn^{2+}}}{C_{Mn^{2+},ref}}\right)^{\frac{-1*\alpha_{c,2}}{2(1-z_{\max})}} \quad [11]$$

$$U_2 = U_2^\theta + \frac{RT}{F}\ln\left[\left(\frac{C_{Zn^{2+}}}{C_{Zn^{2+},ref}}\right)^{\frac{\left(\frac{8}{3}-z_{\max}\right)}{2(1-z_{\max})}}\left(\frac{C_{SO_4^{2-}}}{C_{SO_4^{2-},ref}}\right)^{\frac{\gamma_{Mn,2}\left(\frac{2}{3}\right)}{2(1-z_{\max})}} \times\left(\frac{C_{Mn^{2+}}}{C_{Mn^{2+},ref}}\right)^{\frac{-1}{2(1-z_{\max})}}\right] \quad [12]$$

Reactions 2 and 3 are believed to be reversible, so the transfer anodic and cathodic coefficients were assumed to be 0.5. Because Reaction 1 is expected to be mostly irreversible, anodic ($\alpha_{a,1}$) and cathodic ($\alpha_{a,1}$) transfer coefficients of 0.1 and 0.9 were assumed; mathematically, this decision replicates the irreversible behavior for this reaction. To properly account for unclear elementary reactions, correction terms ($\gamma_{i,j}$) for Reactions 1 and 2 have been included in the model. These correction terms may help identify the stoichiometry of elementary reaction steps. For example, Reaction 1 suggests that the exponent associated with the manganese concentration correction should be 16/45 because this reaction has 16/3 Mn^{2+} atoms per 15 e^-. Hypothetically, if parameter estimation suggests a correction term of 1/4, this would suggest that the limiting elementary reaction likely has a ratio of 4/3 Mn^{2+} atoms per 15 e^-. During parameter estimation, it was found that the experimental data available was unable to statistically identify corrections to the zinc and sulfate exponents, so they were not included in the parameter estimation discussed below.

Insertion reaction empirical parameterization.—As mentioned above, additional care must be taken when developing kinetic and thermodynamic models of a reaction when dealing with a material that undergoes an insertion or extraction reaction, such as the removal of insertion of zinc into the ZMC species. To do so, a technique common to lithium-ion battery models[44,60–63] was employed, in which GITT data are used to construct an open circuit voltage profile that depends on the state of discharge of the material.

Using the voltage values at the end of the hour-long rest step in the GITT procedure, an empirical spline relationship for the open circuit voltage and the relative capacity of the zinc insertion reaction during discharge was fit. For redundancy, this fitting was performed on two separate discharges of a cell, and when normalized for capacity, both experimental discharges agreed closely. The two sets of data were averaged prior to incorporation into the model. The final spline function, and its coefficients can be found in section C of the Supplementary Information. This methodology is visually represented in Fig. 3.

Once fit, one can generate modified Nernst and exchange current density relationships for this reaction, given by Eqs. 13 and 14.

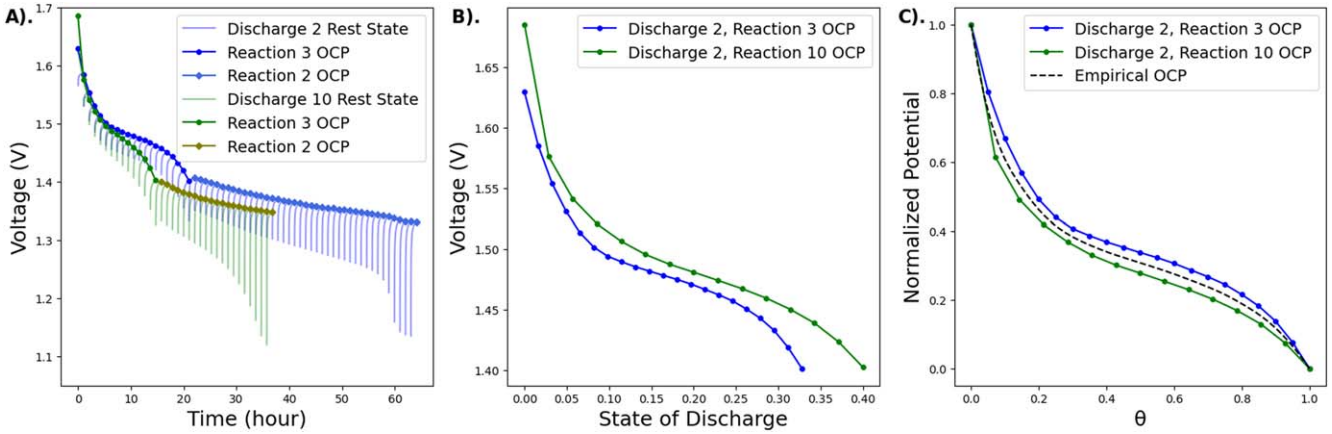

Figure 3. Transformation of GITT open circuit (OCP) data to an empirical spline used for the insertion reaction in the mode. (A) Voltage versus time plot. Both GITT discharges used with point markers indicating the open circuit position in the voltage curve. (B) Voltage versus state of charge plot. The open circuit data point of just the insertion reaction, with an *x*-axis normalized to a state of discharge. (C) Normalized voltage versus theta. A normalized voltage and state of discharge term for the insertion reaction. The dotted black line indicates the average of each experimental curve, and is the one used in this model.

Unlike the relationships above, the following are dependent on amount of zinc in the ZMC material relative to the amount of manganese on a molar basis (denoted by Z) in the ZMC material.

$$i_{o,3} = k_{rxn,3}\left(\frac{C_{Zn^{2+}}}{C_{Zn^{2+},ref}}\right)^{\frac{\alpha_{a,3}}{2}} z^{\alpha_{a,3}}(z_{\max} - z)^{\alpha_{c,3}} \quad [13]$$

$$U_3 = f_{empirical\quad spline}(\theta) + \frac{RT}{F}\ln\left[\left(\frac{C_{Zn^{2+}}}{C_{Zn^{2+},ref}}\right)^{\frac{1}{2}}\right]$$

$$where \quad \theta = \frac{z - z_{\min}}{z_{\max} - z_{\min}} \quad [14]$$

It should be noted here that typically lithium-ion models fit this empirical open circuit voltage as a function of the lithiation of the active material. In said models, this is straightforward because the maximum amount of lithium in the crystal lattice at the end of discharge and the minimum amount at the end of charge are typically known. However, in this case, strong experimental evidence for the minimum amount of zinc (Z_{min}) or maximum amount of zinc (Z_{max}) allowable in ZMC material is lacking. Instead, it is demonstrated that these parameters can be statistically estimated in-silico.

Galvanostatic discharge data.—Each cell was discharged under galvanostatic control at varying rates, and the first five discharges for each are plotted in Fig. 4. For all cells, the first discharge (in blue) exhibits a single voltage plateau associated with the dissolution of pristine Potassium α-MnO_2 (Reaction 1). The second discharge for each (in purple) exhibits three voltage plateaus. The first is the zincation of the ZMC material (Reaction 3), the second is the dissolution of the ZMC material (Reaction 2), and the final is the dissolution of pristine Potassium α-MnO_2 (Reaction 1). The plateau associated with Reaction 1 occurs at a similar voltage to that in the first discharge, but is noticeable shorter, with a plateau capacity of around ~30 mAh g^{-1} as compared to ~400 mAh g^{-1} for the first discharge. This plateau associated with Reaction 1 disappears as the pristine Potassium α-MnO_2 material is irreversibly consumed over the first few cycles, and by the fifth discharge (in red) it is no longer observed.

In Fig. 5, the first and fifth discharge for each discharge rate are plotted together. From this, a few trends stand out. Most obvious is that the voltage of the plateau during the first discharge decreases with increasing rate. This aligns with expectations, and the phenomena can be attributed to increased overpotentials needed to drive the discharge reaction forward. Lower capacities for the first discharge are observed, which is likely due to the overpotentials forcing the cell towards the lower voltage cutoff of 1.1 V earlier in the discharge process. At the first few seconds of the discharge, an expected rapid drop in potential as the cell reaches an overpotential required to drive the reaction forward. However, an unusual voltage rise is also observed for the first ~100 mAh g^{-1}. This slow change is likely due to a shift in open circuit potential of the reaction as the electrolyte composition changes. An expected increase in electrolytic Manganese, a decrease in electrolytic zinc and sulfate as it precipitates into ZHS, and changes in bulk pH of the electrolyte are expected during this period.

The initial voltage before the first discharge is approximately 1.4 V for each cell—this aligns well with the theoretical reversible potential of MnO_2 with a Zn anode Ref.59 From GITT data (Fig. S.2), it is

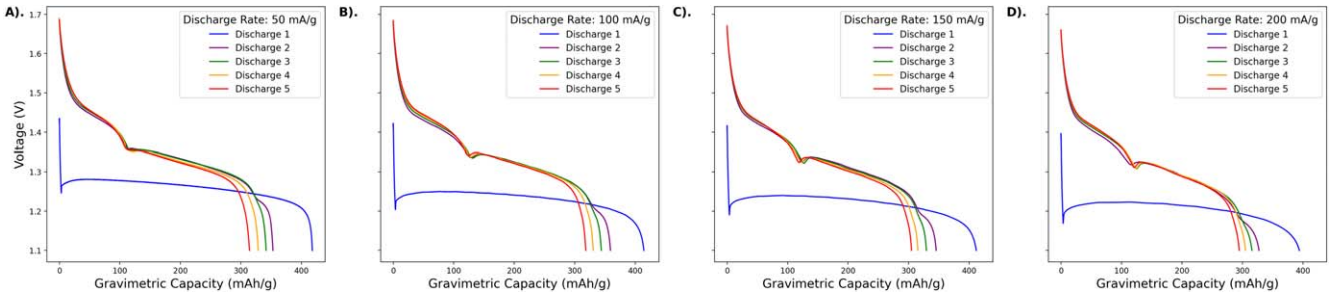

Figure 4. Experimental galvanostatic discharge curves for the first five discharges of each cell. Each subfigure (A through D) is representing a different rate of discharge. The first discharge (blue) is used to for parameter estimates related to Reaction 1, and the fifth discharge (red) is used for parameter estimates related to Reaction 2 and Reaction 3.

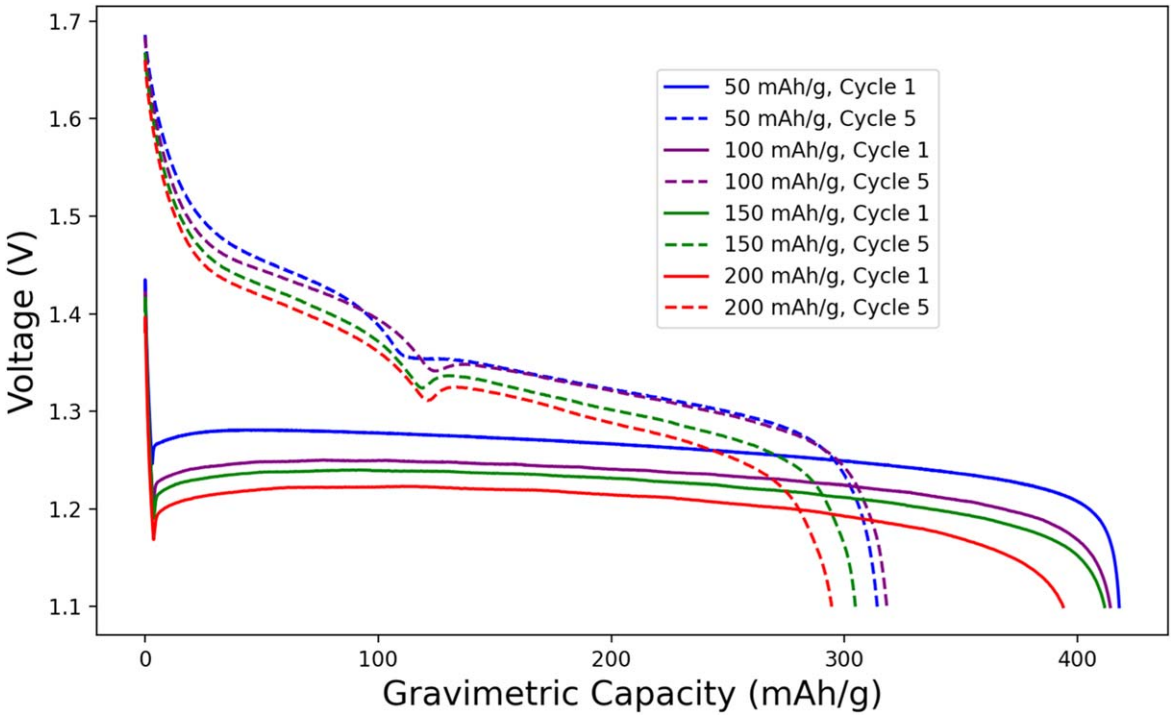

Figure 5. Experimental galvanostatic discharge curves for the first and fifth discharge for discharge rates of 50, 100, 150, and 200 mAh g^{-1}. Line Colors correspond to the discharge rate, the solid lines correspond to the first discharge, and the dashed lines correspond to the fifth discharge.

Table II. The mean and standard deviations of the marginal distributions for each estimated parameter with respect to each discharge rate.

Discharge Rate (mA g^{-1})	$C_{Zn,initial}$ (M)	Z_{min}	Z_{max}	$K_{rxn,1}$ (10^X). (mA cm^{-2})	$K_{rxn,2}$ (10^X) (mA cm^{-2})	$K_{rxn,3}$ (10^X) (mA cm^{-2})	$\gamma_{Mn,1}$	$\gamma_{Mn,2}$
50	1.850 ± 0.002	0.351 ± 0.002	0.594 ± 0.002	−5.653 ± 0.235	−3.839 ± 0.379	−4.156 ± 0.170	0.364 ± 0.153	0.305 ± 0.209
100	1.672 ± 0.003	0.375 ± 0.003	0.640 ± 0.004	−5.727 ± 0.214	−3.345 ± 0.364	−4.021 ± 0.182	0.380 ± 0.146	0.342 ± 0.204
150	1.769 ± 0.002	0.378 ± 0.003	0.635 ± 0.004	−5.757 ± 0.228	−3.333 ± 0.349	−3.932 ± 0.186	0.367 ± 0.149	0.425 ± 0.175
200	1.696 ± 0.002	0.395 ± 0.005	0.660 ± 0.006	−5.839 ± 0.219	−3.393 ± 0.339	−3.897 ± 0.196	0.382 ± 0.140	0.350 ± 0.173
Combined Rates	1.747 ± 0.069	0.375 ± 0.016	0.632 ± 0.024	−5.744 ± 0.234	−3.477 ± 0.415	−4.002 ± 0.209	0.373 ± 0.147	0.355 ± 0.196

evident that the open circuit of Reaction 1 also approaches 1.4 V during the first discharge, so a value of 1.4 V is used in the model as U_1^θ. Similarly, the open circuit voltage of Reaction 2 approaches 1.45 V at the beginning of Reaction 2 (Fig. S.2). Given the similarity to Reaction 1, this is unsurprising, and 1.45 V is used at as U_2^θ in the model.

For the 5th discharge, there is decreased operational voltage with increased discharge rate. This occurs for both the insertion reaction (Reaction 3) from 1.7 V to ~1.4 V and for the dissolution reaction of ZMC (Reaction 2) below ~1.4 V. However, the operating voltage of the Reaction 2 is higher than Reaction 1 despite similar open circuit potentials, suggesting more sluggish kinetics associated with Reaction 1 when compared to Reaction 2, and this assertion is supported in later sections (Table II).

Like Reaction 1, Reaction 2 appears to undergo a voltage rebound after the transition from the Reaction 3 discharge plateau. However this rebound is much shorter in duration, and the depth of the voltage drop seems to increase with reaction rate. This feature may be evidence of a phenomena similar to a 'coup de fouet'[64] in lead-acid chemistries. In lead-acid cells, this transient phenomenon is associated with a supersaturation of an electrolyte and subsequent precipitation of a solid species; this effect also becomes more pronounced at higher discharge rates. In the Zn/MnO_2 system studied here, we hypothesize it is associated with a rise in local pH at the surface of the ZMC material as it dissolves, thus exceeding the pH threshold for the formation of ZHS which subsequently precipitates.

Model agreement for simulated discharges.—Demonstration of model agreement post-parameter estimation is displayed in Figs. 6 and 7. In Fig. 6, the first experimental discharge at each discharge rate is show in subfigures (A) through (D). In Fig. 7, the fifth experimental discharge at each discharge rate is shown. Along with the experimental data is a simulated discharge using the mean parameter estimates, and a confidence interval representing the range of simulations that are observed within one standard deviation of the mean values.

Figure 6 shows that the parameterized simulations are able to capture the voltage behavior well during the second half of the discharge, but they fail to capture the rise in voltage in the first half of the discharge. This suggests that this rise in voltage during the Reaction 1 plateau is likely caused by phenomena that is not modeled in the simulation—namely the effect of pH on the reversible potential of Reaction 1.

The model predicts that the capacity of the first reaction is not limited by the amount of Potassium α-MnO_2 available, but instead the amount of electrolytic Zinc available in the electrolyte. It is expected that that during initial construction of the cell, there is precipitation of ZHS that reduces the concentration of electrolytic zinc. Together, this limiting mode also helps explain why not all the

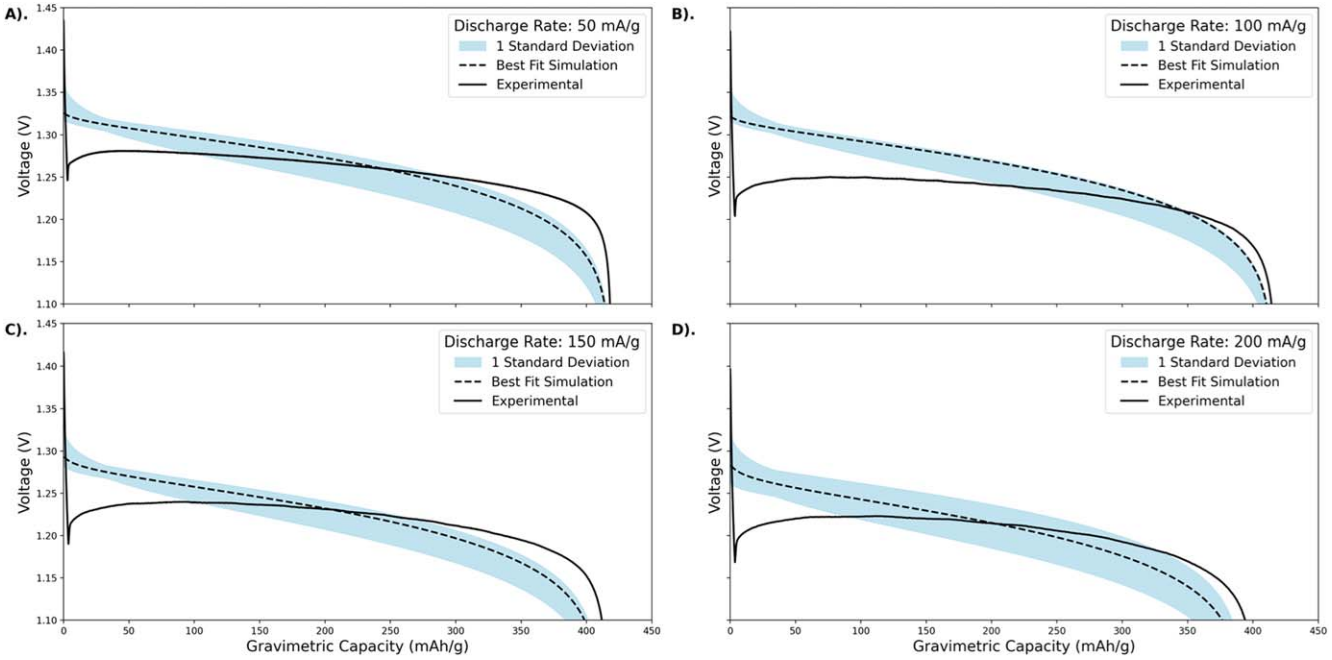

Figure 6. Experimental and mean fit simulation discharge curves for Discharge 1, where only Reaction 1 is occurring. Each subfigure (A through D) is representing a different discharge rate. The solid black lines indicate the experimental data for each discharge rate, and the dotted black line represents the best fit simulation for each discharge rate. The shaded blue region represents a one standard deviation confidence interval from the mean estimates.

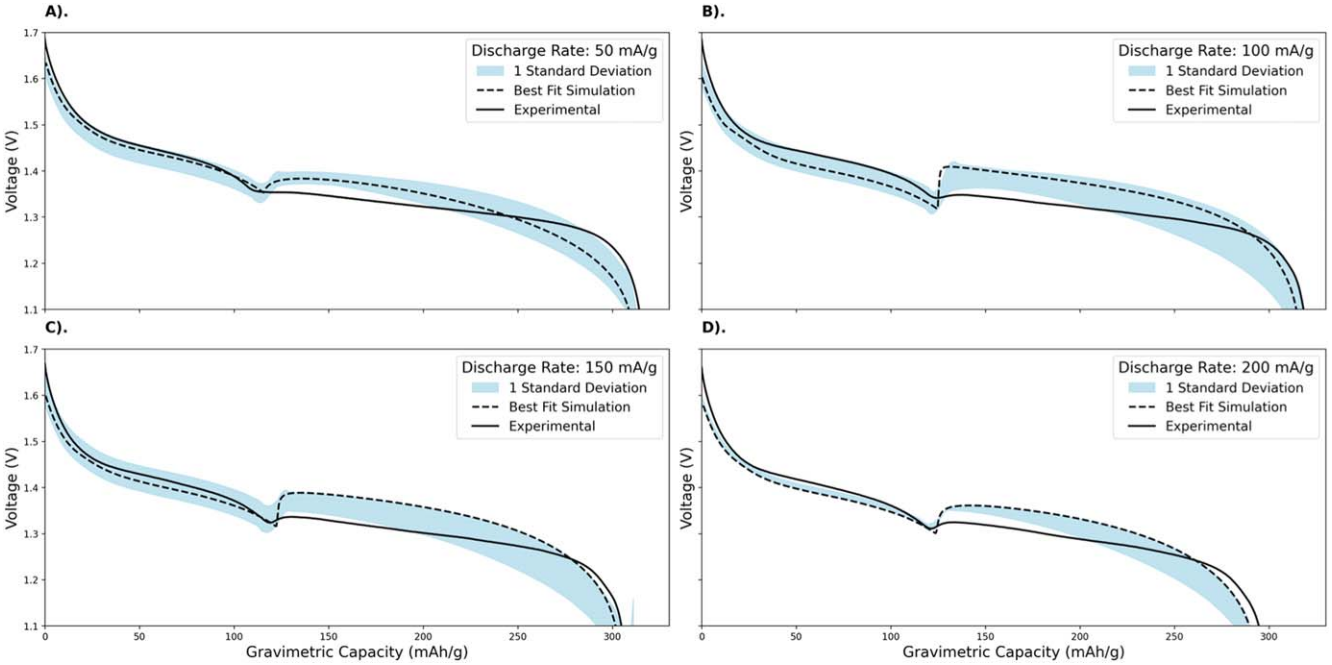

Figure 7. Experimental and mean fit simulation discharge curves for Discharge 5, where only Reaction 2 and 3 are occurring. Each subfigure (A through D) is representing a different discharge rate. The solid black lines indicate the experimental data for each discharge rate, and the dotted black line represents the best fit simulation for each discharge rate. The shaded blue region represents a one standard deviation confidence interval from the mean estimates.

Potassium α-MnO_2 is consumed in the first discharge and why evidence of a Reaction 1 plateau persists through the first few discharges. The parameter estimation methodology slightly underpredicts the capacity of Reaction 1 due to the parameter estimation methodology. This is because the residuals associated with the full voltage curve and the final capacity are equally weighted; in other words, this methodology does not preferentially prefer agreement in capacity or voltage profile. However, this methodology does not account for the fact that some simulated final capacities occur at voltages less than the 1.1 V experimental cutoff. Therefore, parameter estimates exhibit a slight bias towards values that slightly underpredict capacity. This explanation also holds for the Reaction 2 simulation behavior shown in Fig. 7.

Figure 7 shows that the model accurately represents both reactions at all four discharge rates. In each case, there is excellent agreement in terms of voltage profile and capacity for Reaction 3, with the confidence interval entirely encompassing the voltage curve for all estimates. This suggests that the empirical spline fit using

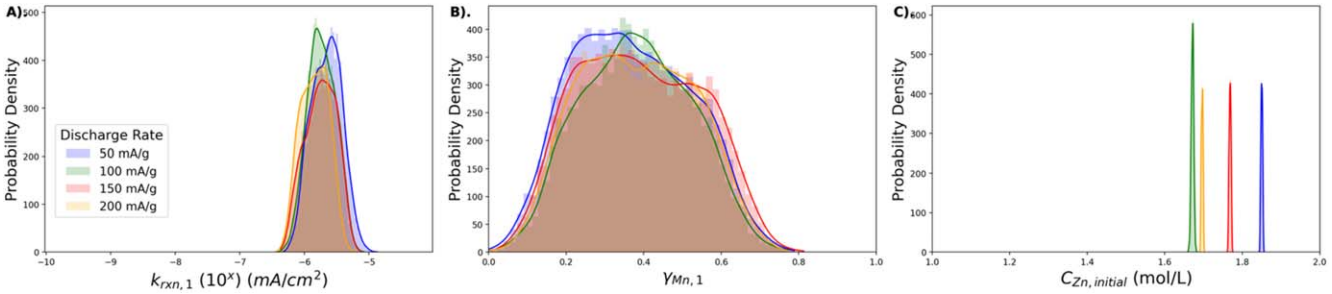

Figure 8. The marginalized probability distributions for (A) the kinetic constant of the pristine material dissolution reaction ($k_{rxn,1}$), (B) the manganese correction term for Reaction 1 ($\gamma_{Mn,1}$), and (C) the initial electrolytic zinc concentration ($C_{Zn,initial}$). Each distribution within a subfigure represents a different discharge rate. The *x*-axis represents the sampled parameter space.

GITT data are representative of this process as a whole, and that there are not significant changes in the mechanism of zinc insertion from rate to rate.

For Reaction 2, the model captures the plateau voltages and capacities well, with most of each experimental curve falling within the confidence band. At the transition point, a small voltage rebounds occurs as the simulation predicts a gradual shift from relying on the insertion reaction to the dissolution reaction as the preferred reaction. The simulation result partially mimics the coup de fouet effect seen in experiment, suggesting that changes in electrolyte composition may partially explain the effect, though not adequately to truly capture the full effect.

The model also predicts a more aggressive voltage slope through the beginning of the Reaction 2 discharge when compared to experiments, but a less aggressive one at the end of discharge. GITT data in Fig. 3a shows that that the open circuit voltage at the end of Reaction 2 is steadily decreasing, and the rapid voltage drop observed at the end of the experimental discharge is due primarily to increases in reaction overpotentials and changes in the open circuit voltage due to off equilibria phenomena such as concentration gradients in the electrolyte. In the model, this behavior is principally governed by a combination of decreasing surface area of the ZMC material, depleted electrolytic zinc, and elevated electrolytic Manganese, each of which may be modeled using incorrect; and further refinements are possible. For example, the model ignores the effects of pH on exchange current density and open circuit potential, and possible impacts ZHS formation on the surface area of ZMC.

Parameter estimation results.—Figure 8 shows the marginal PDFs of the parameters associated with Reaction 1 ($k_{rxn,1}$, $C_{Zn,initial}$, $\gamma_{Mn,1}$). In Fig. 8a, the kinetic constant ($k_{rxn,1}$), is estimated to be $10^{-5.74\ \pm\ 0.23}$ [$mAcm^{-2}$], where the error represents one standard deviation from the mean. For each discharge rate the mean and variance of the distribution is approximately equal, suggesting that this is a good estimate with little rate dependence. This estimate makes intuitive sense, as this term primarily dictates the over-potential needed to drive a reaction forward, and the simulated voltage plateaus in Fig. 6 agree well with experiment. In Fig. 8b, the

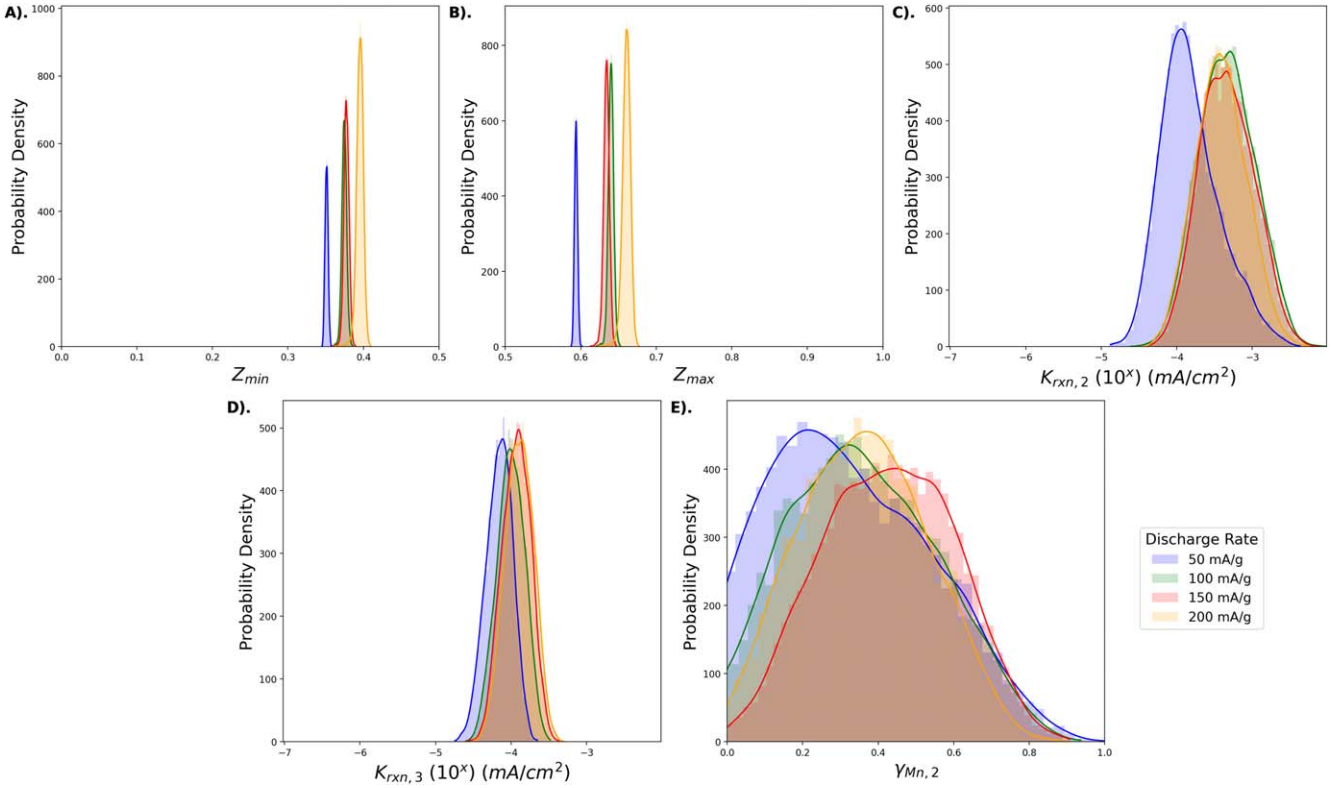

Figure 9. The marginalized probability distributions for (A) the minimum Zn:Mn ratio in ZMC (Z_{min}), (B) the maximum Zn:Mn ratio in ZMC (Z_{max}), (C) the kinetic constant of the ZMC dissolution reaction ($k_{rxn,2}$), (D) the kinetic constant of the ZMC Zn insertion reaction ($k_{rxn,3}$), and (E) the zinc correction term for Reaction 2 ($\gamma_{Mn,2}$). Each distribution within a subfigure represents a different discharge rate. The *x*-axis represents the sampled parameter space.

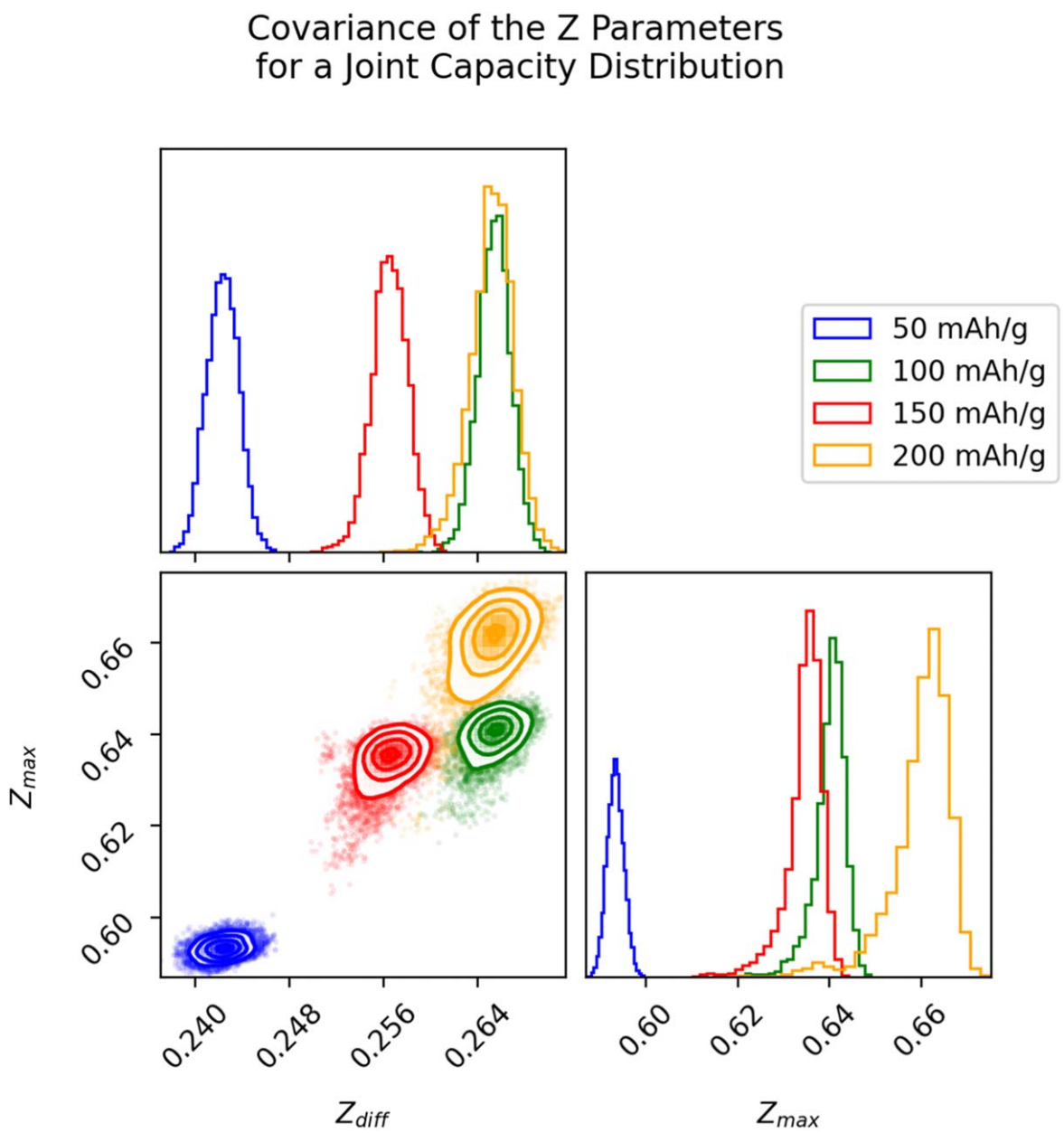

Figure 10. Corner plot for the Z_{diff} and Z_{max} distributions when fitting to the capacity of Reaction 2 and Reaction 3. The colors represent the different cathodes which were discharge at different rates used to generate the distributions. The top and right subplots represent the marginal probabilities of parameters, and the bottom left subplot shows the 2-dimensional distribution.

estimate for the Mn correction term ($\gamma_{Mn,1}$) is 0.373 ± 0.147. Again, the distributions are overlapping, indicating no rate dependence of the estimates. However, the width of the distribution suggests that this estimate is of low precision. This parameter is partially responsible for the voltage sloping behavior during the reaction plateau, so this result is not surprising as the model was unable to capture the initial voltage increase during the first half of the Reaction 1 discharge. However, it is important to note that the estimates here assign an exceedingly low probability to a value of $\gamma_{Mn,1} = 1$, suggesting that the model predicts a lower-than-expected Reaction 1 order dependence on Manganese. Finally, in Fig. 8c the estimates for the initial Zn concentration ($C_{Zn,initial}$) in the electrolyte are precise. This is because depletion of electrolytic zinc is the primary limiting factor governing the capacity of Reaction 1—put simply, Zn is depleted in the electrolyte before available potassium α-MnO_2 is depleted because the formation of ZHS in the cathode outpaces the introduction of zinc at the anode. As a result, this parameter is essentially responsible for determining the final capacity of the reaction, leading to the estimated precision. Altogether, the estimates suggest that $C_{Zn,initial}$ is 1.747 ± 0.070 M, meaning the model expects that approximately 12.5% of the initial electrolytic Zinc is consumed in the formation of ZHS. This may occur spontaneously during cell construction, or during the first discharge provided that it is not driven by the full electrochemical reaction, and only by the reaction outlined in Eq. 7.

Figure 9 shows the marginal PDFs of the parameters associated with Reactions 2 and 3 (Z_{min}, Z_{max}, $k_{rxn,2}$, $k_{rxn,3}$, $\gamma_{Mn,2}$). In Figs. 10a and 10b, the PDFs for the minimum and maximum ratios of Zn:Mn in the ZMC species are given. Together, these two values essentially dictate the capacity of Reaction 2 and 3, so like the $C_{Zn,initial}$ estimates discussed above, these parameters are estimated precisely. The validity of these estimates will be discussed further in a later section. In Figs. 10c and 10D, the estimates for the kinetic constants of Reaction 2 ($k_{rxn,2}$) and Reaction 3 ($k_{rxn,3}$) are given. $k_{rxn,2}$ is estimated to be $10^{-3.48 \pm 0.415}$ [$mAcm^{-2}$] and $k_{rxn,3}$ is estimated to be $10^{-4.00 \pm 0.209}$ [$mAcm^{-2}$]. In both cases, no statistical rate

dependence of these parameters is observed. These values are also roughly 2 orders of magnitude large than the estimate for $k_{rxn,1}$, which supports the earlier assertation that Reaction 1 has comparably slower kinetics. Finally, in Fig. 9e, similar uncertainty in the estimate of $\gamma_{Mn,2}$ is seen when compared to the estimate of $\gamma_{Mn,1}$ in Fig. 8c. For this parameter, overlapping distributions indicated that there is no rate dependence of the estimate.

Table II summarizes the mean and standard deviations of the marginal PDFs for each parameter at each discharge rate. Additionally, it provides a combined estimate, which is calculated by sampling equally from each of the above distributions and taking the mean and standard deviation of these aggregate samples. Corner plots showing parameter covariance and figures showing parameter rate dependence can be found in Figs. S.3 through S.6.

Areas for model improvement.—To build a model of any kind, tradeoffs and assumptions are made; a model should be complex enough to capture the bulk of the relevant phenomena, but not so complex as to be impossible to program, run, parameterize, and interpret. This section discusses known compromises made while constructing this model in the hope that future experimental efforts may help reduce assumptions made.

The first is that there is yet to be consensus on the precise reactions occurring in this system, nor are the authors aware of any attempts to directly determine the relevant elementary reaction steps. The ZMC species stands in for an amorphous compound that is difficult to characterize. Similarly, the ZHS is a layered material that may have a few different hydration states,[19] thus making *ex situ* measurements challenging. Additional solid may exist in the system as well, and more experimental data are needed here.

Accompanying ambiguity in the reaction system, pH effects were not explicitly considered. Solution pH is particularly difficult to model in an aqueous system. The 2 M $ZnSO_4$ electrolyte had a measured pH of 3.95 prior to cell construction. No acid is added to this electrolyte, meaning the acidic pH is due to solvation effects around the Zinc and Sulfate ions. As these concentrations change, and manganese ions and potassium ions are added to the solution as MnO_2 material dissolves, the bulk electrolyte pH is expected to change. Additionally, the consumption of protons during dissolution of MnO_2 (either pristine potassium MnO_2 or amorphous ZMC material) increases the local pH at the surface of the material to mildly basic conditions, at which point ZHS forms and buffers this process. Accurately modeling bulk pH, and the transient gradient of pH to the surface of a material is thus very challenging.

Furthermore, the ZMC compound is not well characterized, and Z_{min} and Z_{max} have not been independently determined. Using energy dispersive spectroscopy (EDS), Lee et al.[35] reported data suggesting the lowest quantities of Zinc in the ZMC material were at the top of charge, and the highest quantities were at the midpoint (~1.4 V). Through parameter estimation, it becomes clear that these values are particularly important when determining reaction capacities, and therefore estimates are highly precise. For Reaction 3, the capacity is determined by the volume fraction of ZMC material in the cathode, and the difference between Z_{min} and Z_{max}, labeled as Z_{diff} in Fig. 10. The covariance between these parameters makes it difficult to jointly estimate. To simplify, the assumption is made that the volume fraction of ZMC is equivalent to the initial volume fraction of potassium MnO_2 (based on the expectation that Manganese entirely returned to a solid form at 1.7 V and does so at a similar density for ZMC as potassium MnO_2). Therefore, the capacity of Reaction 3 is now controlled Z_{diff}.

Similarly, it was found that Reaction 2 could be limited both by depletion of electrolytic zinc and depletion of ZMC in the cathode. Because Z_{max} controls how quickly zinc is consumed (a higher Z_{max} results in faster depletion of electrolytic zinc on a per coulomb basis), Z_{max} also became a mechanism for capacity matching, especially after fixing the amount of ZMC. Equations S.5 and S.12 in the Supplementary Information are derived to determine the capacity of Reaction 3 and 2 respectively and provide a more in-depth discussion on capacity-limiting behavior in the system.

The subplot in the bottom left of Fig. 10 show the 2-dimensional probability distribution, and here the covariance of the Z parameters within each of the four discharge rates is observed to be skewed on the diagonal—this indicated a strong positive covariance between the two parameters. This behavior is expected because the capacity of Reaction 3 is determined Z_{diff}, but the capacity of Reaction 2 is impacted by only Z_{max}. During estimation, this effectively bounds the range for Z_{min}. The four distributions have slightly different optimal Z_{diff} and Z_{max}, though the estimates are all very close. By including the volume fraction of ZMC in the parameter estimation methodology, an attempt could be made to collapse these distributions on top of each, yielding a singular mean value for parameters. However, without a more solid understanding of what the ZMC material(s) is, estimating these parameters with increasing precision is not particularly useful.

Model predictions.—Following the discussion of the known or potential shortcoming of this model, it is useful to check its performance as a predictive tool. Below, model predictions are compared to operando measurements, and some additional predictions suggested by the hypothesized reaction system that are experimentally testable are presented.

Figure 11 compares the simulated electrolytic Manganese concentration (C_{Mn2+}) averaged over the cell to data taken by Wu et al.[29] measured in the separator using Mn fluorescence imaging. In general, the model agrees reasonably with experiment, and the rate of concentration change in the second half of the discharge matches closely with experimental results. However, the model predicts little concentration change during the first half of discharge, disagreeing with the mild increase seem in experiments. This suggests that Manganese dissolution might occur during the period where Reaction 3 is dominant. This may support the hypothesis by Lee et al.[35] that during charge, ZMC forms with high levels of zinc impurities, which are extracted and replaced by manganese atoms above 1.4 V. If the reverse occurs on discharge, this replacement mechanism may be better suited to explain this behavior. This sort of question may be well suited for direct experimental observation.

Another testable prediction made by the model is that there are two capacity-limiting regimes for the dissolution reactions. Generally, at higher volume fractions of ZMC and lower concentrations of Zinc, Reaction 2 is expected to be limited by the depletion of electrolytic zinc. At lower volume fractions of ZMC and higher electrolyte concentrations, Reaction 2 is expected to be limited by the amount of ZMC material that can dissolve. The cells tested in this study sit right on the boundary between the two regimes. Using the theoretical relationships for reaction capacity derived in section E of the Supplementary Information, the boundary of the two capacity-limiting regimes can be estimated. A summarized relationship that can be used to determine whether Reaction 2 is limited by electrolytic zinc is given by Eq. 15. In this equation, the total mass of ZMC in the cathode (m_{zmc}) is compared to the electrolyte volume ($V_{electrolyte}$) and concentration ($C_{Zn^{2+}}$). If it is true, the battery is expected to be limited by electrolytic zinc.

$$\zeta_1 m_{ZMC} > \zeta_2 V_{electrolyte} C_{Zn^{2+}}$$

$$where \quad \zeta_1 = \frac{2(1-Z_{max})}{MW_{ZMC}},\ \zeta_2 = \frac{1}{2}\left(\left(\frac{\frac{8}{3}-Z_{max}}{1-Z_{max}}\right)-1\right) \qquad [15]$$

This relationship may provide guidance for designing an experiment to test the hypothesis that both ZMC volume fractions and electrolytic Zinc concentrations can limit cell capacity. For example, when testing cells with electrolytes ranging 0.1 M to 3 M, one would expect to see an increase in Reaction 2 capacity with increasing zinc concentration until the regime boundary. After the regime boundary, increased electrolytic zinc concentrations would not be expected to yield significant improvements of capacity. Similar capacity behavior would be expected for Reaction 3 in all cases.

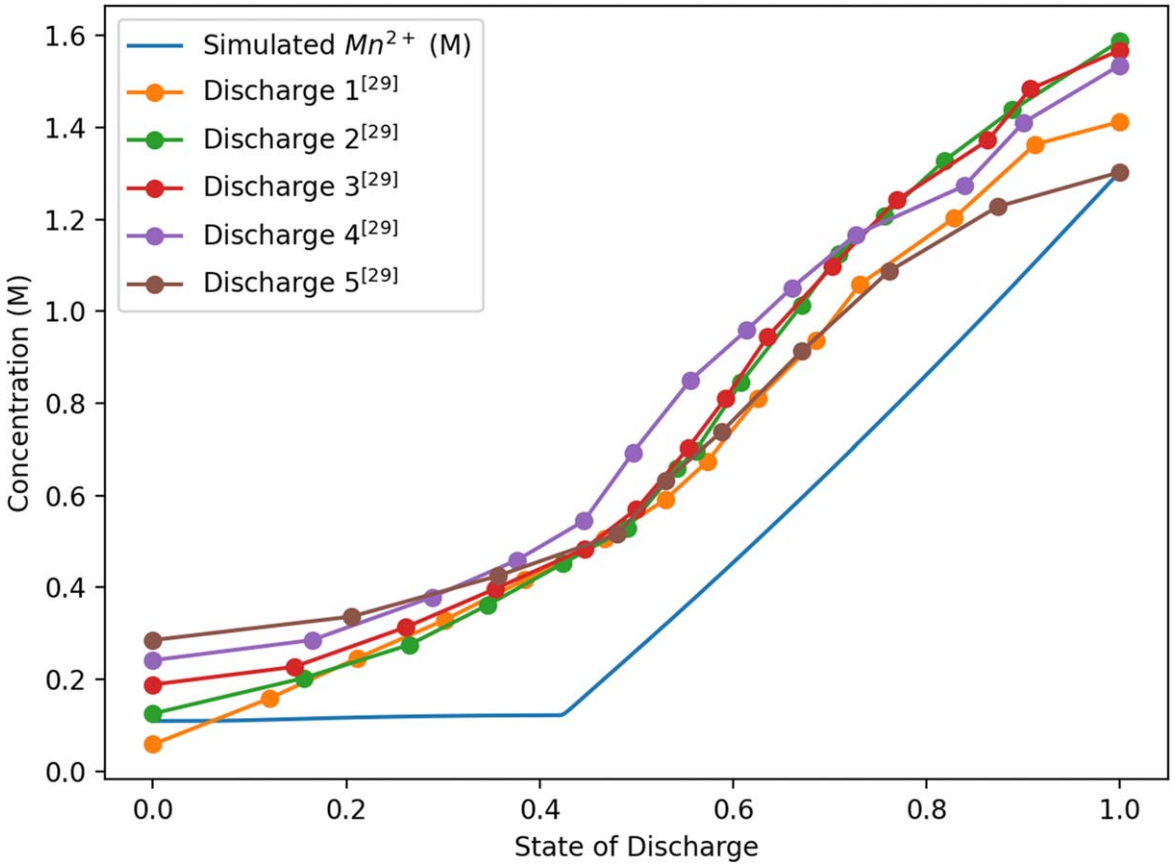

Figure 11. Manganese concentration in the electrolyte during discharge. Experimental data gathered by Wu et al.[29] is compared to simulated data for the best fit data for 5th discharge of the 50 mAh g^{-1} experiment. The simulated data reports the average Manganese concentration in the cathode, and the experimental data shows the measured concentration in a separator.

As mentioned above, a dual-mode capacity limitation is also expected to for Reaction 1. Because the exact quantity of ZMC might not be known, similar tests can be performed on the initial discharge reaction as well where the mass of potassiated α-MnO_2 might be more accurately quantified. In this case spontaneous consumption of electrolytic zinc into ZHS during cell might also bias these results; a reduction of ~12.5% of initial zinc concentration is suggested by the parameter estimates in this work. The general inequality to determine if Reaction 1 is limited by electrolytic zinc is given by Eq. 16, where the total mass of potassiated α-MnO_2 in the cathode ($m_{KMn_8O_{16}}$) is compared to the electrolyte volume ($V_{electrolyte}$) and concentration ($C_{Zn^{2+}}$). If it is true, the battery is expected to be limited by electrolytic zinc.

$$\zeta_1 m_{KMn_8O_{16}} > \zeta_2 V_{electrolyte} C_{Zn^{2+}}$$
$$where \quad \zeta_1 = \frac{15}{MW_{KMn_8O_{16}}}, \zeta_2 = \frac{83}{90} \qquad [16]$$

Conclusions

This work presents a comprehensive framework with which to understand and model the aqueous Zn/MnO_2 rechargeable battery, with a focus on the cathode. A hypothesized reaction system is proposed, which consists of an irreversible pristine material dissolution reaction, the deposition and dissolution of an amorphous zincated Manganese Oxide species, and the insertion/extraction of Zinc from this species. We also include the impact of a pH driven reaction that governs the reversible dissolution and deposition of zinc hydroxide sulfate during cycling. For each case, the kinetic and thermodynamic relationships governing how that specific reaction behaves are derived for the model.

Using this reaction system, a two-domain physics-based continuum model of the battery was developed, borrowing some methodology from previous Li-ion models. Through in-silico parameter estimation, we identified and quantified relevant unknown parameters in model. The model was validated against experimental data, and it was demonstrated that the parameterized model can accurately capture both voltage phenomena during cycling, as well as capacity-limiting behavior and electrolyte changes during cycling. A novel limiting mechanism is also proposed, which is predicted by the model, for the operation of this system—specifically that the depletion of electrolytic zinc during the formation of the ZHS material limits the capacity of the ZMC dissolution reaction. The conditions under which one would expect to see this capacity-limiting mode is outlined, and a method for future testing of this hypothesis is detailed.

Acknowledgments

This research was supported as part of the Center for Mesoscale Transport Properties, an Energy Frontier Research Center supported by the U.S. Department of Energy, Office of Science, Basic Energy Sciences, under award #DE-SC0012673 for financial support. EST acknowledges the William and Jane Knapp Chair of Energy and the Environment.

ORCID

John C. Bernard https://orcid.org/0000-0002-2853-0025
Esther S. Takeuchi https://orcid.org/0000-0001-8518-1047
Amy C. Marschilok https://orcid.org/0000-0001-9174-0474
Kenneth J. Takeuchi https://orcid.org/0000-0001-8129-444X
Alan C. West https://orcid.org/0000-0002-3524-3040

References

1. J. B. Goodenough, "Electrochemical energy storage in a sustainable modern society." *Energy Environ. Sci.*, **7**, 14 (2013).
2. S. Chu and A. Majumdar, "Opportunities and challenges for a sustainable energy future." *Nature*, **488**, 294 (2012).
3. M. Armand and J.-M. Tarascon, "Building better batteries." *Nature*, **451**, 652 (2008).
4. M. R. Shaner, S. J. Davis, N. S. Lewis, and K. Caldeira, "Geophysical constraints on the reliability of solar and wind power in the United States." *Energy Environ. Sci.*, **11**, 914 (2018).
5. G. P. Wheeler, L. Wang, and A. C. Marschilok, *Beyond Li-Ion batteries for grid-scale energy storage* (Cambridge University Press, Cambridge) (2022).
6. C. Xu, B. Li, H. Du, and F. Kang, "Energetic zinc ion chemistry: the rechargeable zinc ion battery." *Angew. Chem. Int. Ed.*, **51**, 933 (2012).
7. N. D. Ingale, J. W. Gallaway, M. Nyce, A. Couzis, and S. Banerjee, "Rechargeability and economic aspects of alkaline zinc–manganese dioxide cells for electrical storage and load leveling." *J. Power Sources*, **276**, 7 (2015).
8. L. E. Blanc, D. Kundu, and L. F. Nazar, "Scientific challenges for the implementation of Zn-Ion batteries." *Joule*, **4**, 771 (2020).
9. M. B. Lim, T. N. Lambert, and B. R. Chalamala, "Rechargeable Alkaline Zinc–Manganese oxide batteries for grid storage: mechanisms, challenges and developments." *Mater. Sci. Eng. R Rep.*, **143**, 100593 (2021).
10. R. M. Wittman, M. L. Perry, T. N. Lambert, B. R. Chalamala, and Y. Preger, "Perspective—On the need for reliability and safety studies of grid-scale aqueous batteries." *J. Electrochem. Soc.*, **167**, 090545 (2020).
11. D. Chao, W. Zhou, F. Xie, C. Ye, H. Li, M. Jaroniec, and S.-Z. Qiao, "Roadmap for advanced aqueous batteries: from design of materials to applications." *Sci. Adv.*, **6**, eaba4098 (2020).
12. H. Pan et al., "Reversible aqueous zinc/manganese oxide energy storage from conversion reactions." *Nat. Energy*, **1**, 1 (2016).
13. C. Xu, H. Du, B. Li, F. Kang, and Y. Zeng, "Reversible insertion properties of zinc ion into manganese dioxide and its application for energy storage." *Electrochem. Solid-State Lett.*, **12**, A61 (2009).
14. W. Sun et al., "Zn/MnO2 battery chemistry with H+ and Zn2+ coinsertion." *J. Am. Chem. Soc.*, **139**, 9775 (2017).
15. P. Oberholzer, E. Tervoort, A. Bouzid, A. Pasquarello, and D. Kundu, "Oxide versus nonoxide cathode materials for aqueous zn batteries: an insight into the charge storage mechanism and consequences thereof." *ACS Appl. Mater. Interfaces*, **11**, 674 (2019).
16. W. Liu, X. Zhang, Y. Huang, B. Jiang, Z. Chang, C. Xu, and F. Kang, "β-MnO2 with proton conversion mechanism in rechargeable zinc ion battery." *J. Energy Chem.*, **56**, 365 (2021).
17. M. H. Alfaruqi, V. Mathew, J. Gim, S. Kim, J. Song, J. P. Baboo, S. H. Choi, and J. Kim, "Electrochemically induced structural transformation in a γ-MnO2 cathode of a high capacity zinc-ion battery system." *Chem. Mater.*, **27**, 3609 (2015).
18. B. Lee, C. S. Yoon, H. R. Lee, K. Y. Chung, B. W. Cho, and S. H. Oh, "Electrochemically-induced reversible transition from the tunneled to layered polymorphs of manganese dioxide." *Sci. Rep.*, **4**, 6066 (2014).
19. B. Lee, H. R. Lee, H. Kim, K. Y. Chung, B. W. Cho, and S. H. Oh, "Elucidating the intercalation mechanism of zinc ions into α-MnO2 for rechargeable zinc batteries." *Chem. Commun.*, **51**, 9265 (2015).
20. N. Zhang, F. Cheng, Y. Liu, Q. Zhao, K. Lei, C. Chen, X. Liu, and J. Chen, "Cation-Deficient spinel ZnMn2O4 cathode in Zn(CF3SO3)2 electrolyte for rechargeable aqueous Zn-ion battery." *J. Am. Chem. Soc.*, **138**, 12894 (2016).
21. N. Zhang, F. Cheng, J. Liu, L. Wang, X. Long, X. Liu, F. Li, and J. Chen, "Rechargeable aqueous zinc-manganese dioxide batteries with high energy and power densities." *Nat. Commun.*, **8**, 405 (2017).
22. S. Zhao, B. Han, D. Zhang, Q. Huang, L. Xiao, L. Chen, D. G. Ivey, Y. Deng, and W. Wei, "Unravelling the reaction chemistry and degradation mechanism in aqueous Zn/MnO2 rechargeable batteries." *J. Mater. Chem. A*, **6**, 5733 (2018).
23. J. Huang, Z. Wang, M. Hou, X. Dong, Y. Liu, Y. Wang, and Y. Xia, "Polyaniline-intercalated manganese dioxide nanolayers as a high-performance cathode material for an aqueous zinc-ion battery." *Nat. Commun.*, **9**, 2906 (2018).
24. Y. Huang, J. Mou, W. Liu, X. Wang, L. Dong, F. Kang, and C. Xu, "Novel insights into energy storage mechanism of aqueous rechargeable Zn/MnO2 batteries with participation of Mn2+." *Nano-Micro Lett.*, **11**, 49 (2019).
25. X. Gao, H. Wu, W. Li, Y. Tian, Y. Zhang, H. Wu, L. Yang, G. Zou, H. Hou, and X. H. Ji, "+-Insertion boosted α-MnO2 for an aqueous Zn-ion battery." *Small*, **16**, 1905842 (2020).
26. G. Fang, C. Zhu, M. Chen, J. Zhou, B. Tang, X. Cao, X. Zheng, A. Pan, and S. Liang, "Suppressing manganese dissolution in potassium manganate with rich oxygen defects engaged high-energy-density and durable aqueous zinc-ion battery." *Adv. Funct. Mater.*, **29**, 1808375 (2019).
27. J. Lei, Y. Yao, Z. Wang, and Y.-C. Lu, "Towards high-areal-capacity aqueous zinc–manganese batteries: promoting MnO2 dissolution by redox mediators." *Energy Environ. Sci.*, **14**, 4418 (2021).
28. X. Guo, J. Zhou, C. Bai, X. Li, G. Fang, and S. Liang, "Zn/MnO2 battery chemistry with dissolution-deposition mechanism." *Mater. Today Energy*, **16**, 100396 (2020).
29. D. Wu et al., "Quantitative temporally and spatially resolved X-ray fluorescence microprobe characterization of the manganese dissolution-deposition mechanism in aqueous Zn/α-MnO2 batteries." *Energy Environ. Sci.*, **13**, 4322 (2020).
30. S. J. Kim, D. Wu, L. M. Housel, L. Wu, K. J. Takeuchi, A. C. Marschilok, E. S. Takeuchi, and Y. Zhu, "Toward the understanding of the reaction mechanism of Zn/MnO2 batteries using non-alkaline aqueous electrolytes." *Chem. Mater.*, **33**, 7283 (2021).
31. O. Fitz, C. Bischoff, M. Bauer, H. Gentischer, K. P. Birke, H.-M. Henning, and D. Biro, "Electrolyte study with in operando pH tracking providing insight into the reaction mechanism of aqueous acidic Zn//MnO2 batteries." *ChemElectroChem*, **8**, 3553 (2021).
32. M. Mateos, K. R. Harris, B. Limoges, and V. Balland, "Nanostructured electrode enabling fast and fully reversible MnO2 -to-Mn2+ conversion in mild buffered aqueous electrolytes." *ACS Appl. Energy Mater.*, **3**, 7610 (2020).
33. M. Wang, X. Zheng, X. Zhang, D. Chao, S.-Z. Qiao, H. N. Alshareef, Y. Cui, and W. Chen, "Opportunities of aqueous manganese-based batteries with deposition and stripping chemistry." *Adv. Energy Mater.*, **11**, 2002904 (2021).
34. J. Yang, J. Cao, Y. Peng, W. Yang, S. Barg, Z. Liu, I. A. Kinloch, M. A. Bissett, and R. A. W. Dryfe, "Unravelling the mechanism of rechargeable aqueous Zn–MnO2 batteries: implementation of charging process by electrodeposition of MnO2." *ChemSusChem*, **13**, 4103 (2020).
35. B. Lee, J. Choi, M. Lee, S. Han, M. Jeong, T. Yim, and S. Hyoung Oh, "Unraveling the critical role of Zn-phyllomanganates in zinc ion batteries." *J. Mater. Chem. A*, **9**, 13950 (2021).
36. H. Moon et al., "Direct proof of the reversible dissolution/deposition of Mn2+/Mn4+ for mild-acid Zn-MnO2 batteries with porous carbon interlayers." *Adv. Sci.*, **8**, 2003714 (2021).
37. D. Wu et al., "Simultaneous elucidation of solid and solution manganese environments via multiphase operando extended X-ray absorption fine structure spectroscopy in aqueous Zn/MnO2 batteries." *J. Am. Chem. Soc.*, **144**(51), 23405-23420 (2022), (10.1021/jacs.2c09477).
38. J. Luo, H. T. Zhu, H. M. Fan, J. K. Liang, H. L. Shi, G. H. Rao, J. B. Li, Z. M. Du, and Z. X. Shen, "Synthesis of single-crystal tetragonal α-MnO2 nanotubes." *J. Phys. Chem. C*, **112**, 12594 (2008).
39. J. Huang et al., "Potassium-containing α-MnO2 nanotubes: the impact of hollow regions on electrochemistry." *J. Electrochem. Soc.*, **168**, 090559 (2021).
40. J. S. Newman and N. P. Balsara, *Electrochemical Systems* 4th ed.(Wiley, Hoboken, NJ) (2019).
41. S. J. Kim, D. Wu, N. Sadique, C. D. Quilty, L. Wu, A. C. Marschilok, K. J. Takeuchi, E. S. Takeuchi, and Y. Zhu, "Unraveling the dissolution-mediated reaction mechanism of α-MnO2 cathodes for aqueous Zn-Ion batteries." *Small*, **16**, 2005406 (2020).
42. Z. R. Mansley, Y. Zhu, D. Wu, E. S. Takeuchi, A. C. Marschilok, L. Wang, and K. J. Takeuchi, "Mechanism of chalcophanite nucleation in zinc hydroxide sulfate cathodes in aqueous zinc batteries." *Nano Lett.*, **23**(18), 8657-8663 (2023-09-27), (10.1021/acs.nanolett.3c02430).
43. N. W. Brady, C. A. Gould, and A. C. West, "Quantitative parameter estimation, model selection, and variable selection in battery science." *J. Electrochem. Soc.*, **167**, 013501 (2019).
44. K. S. Mayilvahanan et al., "Quantifying uncertainty in tortuosity estimates for porous electrodes." *J. Electrochem. Soc.*, **168**, 070537 (2021).
45. I. M. Sobol, "On the distribution of points in a cube and the approximate evaluation of integrals." *USSR Comput. Math. Math. Phys.*, **7**, 86 (1967).
46. E. Parzen, "On estimation of a probability density function and mode." *Ann. Math. Stat.*, **33**, 1065 (1962).
47. R. van de Schoot et al., "Bayesian statistics and modelling." *Nat. Rev. Methods Primer*, **1**, 1 (2021).
48. K. Momma and F. Izumi, "VESTA 3 for three-dimensional visualization of crystal, volumetric and morphology data." *J. Appl. Crystallogr.*, **44**, 1272 (2011).
49. J. Chen, X. Tang, J. Liu, E. Zhan, J. Li, X. Huang, and W. Shen, "Synthesis and characterization of Ag−hollandite nanofibers and its catalytic application in ethanol oxidation." *Chem. Mater.*, **19**, 4292 (2007).
50. H. Huang, Y. Meng, A. Labonte, A. Dobley, and S. L. Suib, "Large-scale synthesis of silver manganese oxide nanofibers and their oxygen reduction properties." *J. Phys. Chem. C*, **117**, 25352 (2013).
51. D. Wu et al., "Operando investigation of aqueous zinc manganese oxide batteries: multi-stage reaction mechanism revealed." *J. Mater. Chem. A*, **11**, 16279 (2023).
52. S. W. Baek, M. Saber, A. Van der Ven, and L. Pilon, "Thermodynamic analysis and interpretative guide to entropic potential measurements of lithium-ion battery electrodes." *J. Phys. Chem. C*, **126**, 6096 (2022).
53. M. Chandesris, D. Caliste, D. Jamet, and P. Pochet, "Thermodynamics and related kinetics of staging in intercalation compounds." *J. Phys. Chem. C*, **123**, 23711 (2019).
54. D. K. Karthikeyan, G. Sikha, and R. E. White, "Thermodynamic model development for lithium intercalation electrodes." *J. Power Sources*, **185**, 1398 (2008).
55. M. D. Levi and D. Aurbach, "Frumkin intercalation isotherm — a tool for the description of lithium insertion into host materials: a review." *Electrochim. Acta*, **45**, 167 (1999).
56. A. Van der Ven, J. Bhattacharya, and A. A. Belak, "Understanding Li diffusion in Li-intercalation compounds." *Acc. Chem. Res.*, **46**, 1216 (2013).
57. B. Lee, H. R. Seo, H. R. Lee, C. S. Yoon, J. H. Kim, K. Y. Chung, B. W. Cho, and S. H. Oh, "Critical role of pH evolution of electrolyte in the reaction mechanism for rechargeable zinc batteries." *ChemSusChem*, **9**, 2948 (2016).
58. C. F. Bischoff, O. S. Fitz, J. Burns, M. Bauer, H. Gentischer, K. P. Birke, H.-M. Henning, and D. Biro, "Revealing the local pH value changes of acidic aqueous zinc ion batteries with a manganese dioxide electrode during cycling." *J. Electrochem. Soc.*, **167**, 020545 (2020).

59. O. Rubel, T. N. T. Tran, S. Gourley, S. Anand, A. Van Bommel, B. D. Adams, D. G. Ivey, and D. Higgins, "Electrochemical stability of ZnMn2O4: understanding zn-ion rechargeable battery capacity and degradation." *J. Phys. Chem. C*, **126**, 10957 (2022).
60. N. W. Brady, Q. Zhang, K. W. Knehr, P. Liu, A. C. Marschilok, K. J. Takeuchi, E. S. Takeuchi, and A. C. West, "Discharge, relaxation, and charge model for the lithium trivanadate electrode: reactions, phase change, and transport." *J. Electrochem. Soc.*, **163**, A2890 (2016).
61. J. C. Bernard, J. C. Hestenes, K. S. Mayilvahanan, L. E. Marbella, and A. C. West, "Investigating the influence of polymer binders on liquid phase transport and tortuosity through lithium-ion electrodes." *J. Electrochem. Soc.*, **170**, 030518 (2023).
62. Z. Hui, K. S. Mayilvahanan, Y. Yang, and A. C. West, "Determining the length scale of transport impedances in li-ion electrodes: Li(Ni0.33Mn0.33Co0.33)O2." *J. Electrochem. Soc.*, **167**, 100542 (2020).
63. K. W. Knehr, N. W. Brady, C. A. Cama, D. C. Bock, Z. Lin, C. N. Lininger, A. C. Marschilok, K. J. Takeuchi, E. S. Takeuchi, and A. C. West, "Modeling the mesoscale transport of lithium-magnetite electrodes using insight from discharge and voltage recovery experiments." *J. Electrochem. Soc.*, **162**, A2817 (2015).
64. P. E. Pascoe and A. H. Anbuky, "The behaviour of the coup de fouet of valve-regulated lead–acid batteries." *J. Power Sources*, **111**, 304 (2002).